

THE K2 GALACTIC ARCHAEOLOGY PROGRAM DATA RELEASE 1: ASTEROSEISMIC RESULTS FROM CAMPAIGN 1

DENNIS STELLO^{1,2,3}, JOEL ZINN⁴, YVONNE ELSWORTH^{5,2}, RAFAEL A. GARCIA⁶, THOMAS KALLINGER⁷, SAVITA MATHUR⁸, BENOIT MOSSER⁹, SANJIB SHARMA², WILLIAM J. CHAPLIN^{5,2}, GUY DAVIES^{5,2}, DANIEL HUBER^{2,3,10}, CAITLIN D. JONES^{5,2}, ANDREA MIGLIO^{5,2}, VICTOR SILVA AGUIRRE³

Draft version December 1, 2016

ABSTRACT

NASA’s K2 mission is observing tens of thousands of stars along the ecliptic, providing data suitable for large scale asteroseismic analyses to inform galactic archaeology studies. Its first campaign covered a field near the north galactic cap, a region never covered before by large asteroseismic-ensemble investigations, and was therefore of particular interest for exploring this part of our Galaxy. Here we report the asteroseismic analysis of all stars selected by the K2 Galactic Archaeology Program during the mission’s “North Galactic Cap” campaign 1. Our consolidated analysis uses six independent methods to measure the global seismic properties, in particular the large frequency separation, and the frequency of maximum power. From the full target sample of 8630 stars we find about 1200 oscillating red giants, a number comparable with estimates from galactic synthesis modeling. Thus, as a valuable by-product we find roughly 7500 stars to be dwarfs, which provide a sample well suited for galactic exoplanet occurrence studies because they originate from our simple and easily reproducible selection function. In addition, to facilitate the full potential of the data set for galactic archaeology we assess the detection completeness of our sample of oscillating red giants. We find the sample is at least near complete for stars with $40 \lesssim \nu_{\max}/\mu\text{Hz} \lesssim 270$, and $\nu_{\max,\text{detect}} < 2.6 \times 10^6 \cdot 2^{-Kp} \mu\text{Hz}$. There is a detection bias against helium core burning stars with $\nu_{\max} \sim 30 \mu\text{Hz}$, affecting the number of measurements of $\Delta\nu$ and possibly also ν_{\max} . Although we can detect oscillations down to $Kp = 15$, our campaign 1 sample lacks enough faint giants to assess the detection completeness for stars fainter than $Kp \sim 14.5$.

Subject headings: stars: fundamental parameters — stars: oscillations — stars: interiors — planetary systems

1. INTRODUCTION

From the birth of *Kepler*’s second-life mission, K2 (Howell et al. 2014), grew the K2 Galactic Archaeology Program (GAP) (Stello et al. 2015). With this program we aim to measure convectively-driven, or solar-like, oscillations in tens of thousands of red giants using the high-precision photometry from K2. The asteroseismic imprint in the data combined with ground-based measurements of effective temperature and metallicity will allow us to infer stellar properties such as radius and mass, and hence distance and age, even for stars out to a few tens of kilo parsec (Mathur et al. 2016). This in turn will enable us to probe the structure and evolution of vast regions of the Galaxy not probed before by asteroseismic means (e.g. Miglio et al. 2012). It has become clear that the power of such seismic-inferred galactic studies, depends

strongly on how well we understand the target selection and the detection biases involved (Sharma et al. 2016). The K2 GAP target selection has been particularly designed to gain full control of the selection bias, and hence to mitigate some of the problems encountered using stars from CoRoT or the original *Kepler* mission. However, for the program to reach its full potential we also need to be able to predict any detection bias in the asteroseismology in order to make robust inferences based on galactic model comparisons.

In this paper, we present the seismic analysis of all stars selected by the K2 GAP in campaign 1 (C1), and release, to the community, the full seismic data set of the large frequency separation, $\Delta\nu$, and the frequency of maximum power, ν_{\max} . After an initial description of the target selection (Sect. 2), we give a brief overview of the methods used to measure the seismic properties (Sect.3), before presenting the results in Sect. 4. In Sect. 5 we assess the detection bias and its effect on the sample completeness before concluding in Sect. 6.

2. CAMPAIGN-1 TARGET SELECTION AND OBSERVATIONS

Our prime targets are red giants. The advantage of red giants is that they are intrinsically bright and show larger amplitude oscillations compared to dwarfs. Oscillations can therefore be detected even for distant stars. Most giants also oscillate with frequencies that are well sampled by K2’s main, long cadence, observation mode. This enables large numbers of stars to be observed as required to perform robust stellar population studies.

2.1. Target selection strategy

We deliberately follow a simple color-magnitude target selection to ensure reproducibility and to strengthen the synergy with the selection criteria of large-scale high-resolution

¹ School of Physics, University of New South Wales, NSW 2052, Australia

² Sydney Institute for Astronomy (SIFA), School of Physics, University of Sydney, NSW 2006, Australia

³ Stellar Astrophysics Centre, Department of Physics and Astronomy, Aarhus University, Ny Munkegade 120, DK-8000 Aarhus C, Denmark

⁴ Department of Astronomy, The Ohio State University, Columbus, OH 43210, USA

⁵ School of Physics & Astronomy, University of Birmingham, Edgbaston, Birmingham, B15 2TT, UK

⁶ Laboratoire AIM, CEA/DSM – CNRS – Univ. Paris Diderot – IRFU/SAP, Centre de Saclay, 91191 Gif-sur-Yvette Cedex, France

⁷ Institute of Astrophysics, University of Vienna, Trkenschanzstrasse 17, Vienna 1180, Austria

⁸ Center for Extrasolar Planetary Systems, Space Science Institute, 4750 Walnut street Suite 205 Boulder, CO 80301 USA

⁹ LESIA, Observatoire de Paris, PSL Research University, CNRS, Université Pierre et Marie Curie, Université Paris Diderot, 92195 Meudon, France cedex, France

¹⁰ SETI Institute, 189 Bernardo Avenue, Mountain View, CA 94043, USA

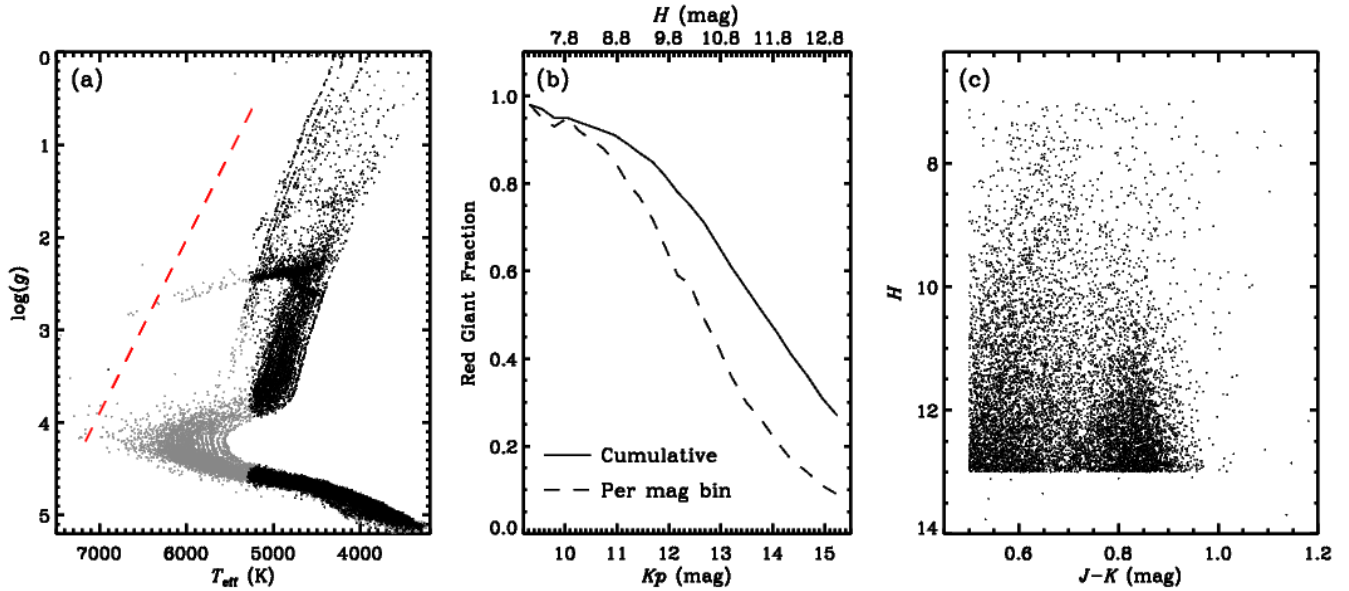


FIG. 1.— (a) Kiel diagram of a synthesis population of the K2 C1 stars based on a *Galaxia* simulation (Sect. 2.2). Black symbols show stars that fulfill the K2 GAP selection criteria. The dashed red line indicate the approximate location of the red edge of the classical instability strip. (b) Estimated giant fraction of K2 GAP targets per magnitude bin (dashed) and cumulative going from bright to faint (solid), based on a *Galaxia* simulation. The approximate H -band magnitude is shown on the top axis. (c) Color-magnitude diagram of stars observed by K2 during C1 that were selected from the K2 GAP target list.

spectroscopic surveys from ground such as APOGEE (Majewski et al. 2010), and Galah (De Silva et al. 2015). Specifically, for C1 (proposal GO1059)¹¹ we selected all stars with $J - K > 0.5$ and $7 < H < 13$ using 2MASS, and sorted our target list by H -band magnitude (Skrutskie et al. 2006)¹². Stars with $J - K > 0.5$ already observed by APOGEE (258) and RAVE (another 147) at the time of target selection were bumped up as top priority targets, and for those we allowed the eight stars fainter than $H = 13$ to enter our list. Figure 1a shows $\log g$ versus T_{eff} for a synthesized population of stars representative of the K2 C1 field, which we generated using the *Galaxia* Milky Way synthesis tool (Sharma et al. 2011). We have highlighted the stars that follow the K2 GAP selection function. It illustrates how our color-cut is the sweet spot to ensure we do not lose many helium-core burning red giants while not including too many main sequence and sub-giant stars for which we can not detect oscillations with K2’s long cadence mode. Figure 1b shows the expected giant fraction based on the *Galaxia* simulation, and Figure 1c shows the color-magnitude diagram of the K2-GAP-selected stars that were observed by K2.

Of the total 21,648 C1 targets observed by K2, 8,630 are on the K2 GAP target list. This number is further broken down into 8,385 stars explicitly sourced from our target list, hence following our selection approach, and 245 serendipitous stars sourced from other K2 observing programs, which are therefore following a different, and rather complex, selection function. We further note that there were 155 stars, randomly distributed in priority, among our top 8,540 ranked targets, which were not observed, hence resulting in the 8,385 observed K2 GAP-selected stars in total. The missing 155 stars represent an unbiased set, which were deselected by the mission be-

cause they, or a saturated neighbor, were deemed too close to an edge of active silicon on the detector. Hence, they do not cause concern in terms of biasing the selection function. In summary, our color-magnitude selection can be regarded complete down to $H = 12.9$, corresponding to 14.5-16.5 in the *Kepler* band-pass, K_p , depending on color.

All K2 GAP targets were observed in the spacecraft’s 29.4 minute long cadence mode for about 80 days from 2014 May 30 to 2014 Aug 21. We adopted the light curves from Vanderburg & Johnson (2014) and Vanderburg et al. (2015), which we high-pass filtered and gap-filled following the approach by Stello et al. (2015). This approach should minimise the artifacts in the data caused by the near-regular firing of the on-board thrusters used to stabilise the spacecraft roll angle every 6-hrs.

2.2. Synergy with exoplanet research

Our color-magnitude selection is expected to include a significant fraction of dwarfs and subgiants, particularly for high Galactic latitude fields like C1 (Figure 1b). Due to the simplicity of the selection function, these dwarfs and subgiants will form a unique subset to study exoplanet occurrence rates as a function of different stellar populations in our galaxy. The giant-dwarf classifications provided by our program will also be valuable to prevent biases when calculating planet occurrence rates, which sensitively depend on stellar classifications (Burke et al. 2015).

Our subsequent seismic analysis will show oscillations only in stars with roughly $1.9 < \log g < 3.2$ (Stello et al. 2015), but for stars with $\log g < 1.9$ we can expect to see the signature of granulation, which will reveal that they are intrinsically bright giants (Sect. 3). Hence, the stars with no detected oscillations or granulation will most likely be the dwarfs and subgiants that could be used for exoplanet occurrence rate studies. From a population synthesis model of our C1 selection using *Galaxia* (Sharma et al. 2011) we expect our sample to include about 7500 stars with $\log g > 3.2$, almost all dwarfs

¹¹ <http://keplerscience.arc.nasa.gov/index.shtml>

¹² Stars were selected only if 2MASS bflag=1, cflag=0, xflag=0, aflag=0, prox > 6.0, and photometry quality flags (qflag) equal to A or B. See 2MASS website, vizier 2MASS table, or the APOGEE target selection paper by Zaborowski et al. (2013) for more information on flags.

($\log g > 4.2$) and only about 100 subgiant and low luminosity red giant branch stars ($3.2 < \log g < 4.2$) (see Sect. 4).

3. APPROACH AND METHODS

The range of oscillation frequencies detectable from a single campaign of K2 data is set by the length and the sampling rate of the time series, which defines the lower and upper frequency limits, respectively. These correspond to a range in ν_{\max} of ~ 10 -270 μHz (Stello et al. 2015), or roughly $1.9 < \log g < 3.2$. Because our selection approach includes stars outside this range, and because it is critical to understand the seismic detection bias for galactic archaeology purposes, it becomes particularly important that we assess robustly if a star is a giant, with $10 < \nu_{\max}/\mu\text{Hz} < 270$, or not.

We receive 4,000-10,000 new K2 GAP targets for each campaign. With this rate of new stars to be analysed, and the need to robustly determine which of them are giants, calls for a new approach to analyse and consolidate the seismic results compared to previous analyses based on the *Kepler* field. Those analyses were focusing on providing measurements of stars that were clearly showing oscillations, assessed by the level of agreement between results from independent methods (Hekker et al. 2011a, 2012; Pinsonneault et al. 2014). This approach is prone to favour/select stars with the clearest detections rather than selecting all stars, introducing a bias that is difficult to mimic in subsequent comparisons with galactic synthesis models.

Here we use six independent analysis pipelines (called CAN, COR, BHM, A2Z, SYD, and BAM)¹³ to analyse the light curves in order to extract the large frequency separation, $\Delta\nu$, and the frequency of maximum power, ν_{\max} (see e.g. Kjeldsen & Bedding 1995; Chaplin & Miglio 2013, for more discussion on those two observables). Except for BHM, we also measure the amplitude of the oscillations, or some equivalent measure of oscillation strength for validation purposes. Pipeline leads were asked to only return results that they trusted, because comparisons between pipelines would not be used to remove outliers. Instead, we rely on the combined set of results from all pipelines to generate a list of stars for which at least one pipeline was able to detect oscillations (meaning at least measure ν_{\max}), and for that set to make careful visual inspections to verify if the stars indeed show signs of oscillations or granulation in the power spectrum.

3.1. Pipelines

In the following we describe briefly each pipeline and how some of them used post processing criteria to select the final sample of stars believed to show oscillations. It should be stressed that only three pipelines (CAN, BHM, and BAM) determine the likelihood of a star showing oscillations based purely on the power and time scale of the seismic (and granulation) signal. The others require a clear presence of a regular frequency pattern, from which $\Delta\nu$ can be measured. The latter is a more strict criterion and hence leads to fewer detections of oscillating stars.

CAN uses the following Bayesian nested-sampling-based scheme for the fitting and estimation of the measurement uncertainties. First, the ‘typical’ time scale in the time series is found by fitting a sinc function to the auto-correlation function (ACF) of the time series (Kallinger et al. 2016), and a χ^2 goodness of fit test is carried out. Then, it is evaluated if the rms of the time series is within a factor of five from the

expected value given the ACF timescale, which makes use of an empirical rms-time scale relation (analogous to using an amplitude- ν_{\max} relation). If a star passes both the goodness of fit test and fall within the rms-time scale relation, it is accepted as a ‘red giant candidate’, for which the following, and most restrictive, step is performed. By fitting the power spectrum with and without a Gaussian (to account for an oscillation power excess) on top of the background, the Bayesian model evidence determines if the power excess is statistically significant or not. Here, the range in ν_{\max} for the location of the Gaussian is guided by the ACF time scale (Kallinger et al. 2016). If a star is deemed to not show any significant power excess implies that the ν_{\max} from the fit cannot be trusted and the star is deemed a non-detection. To tension the number of accepted false positive against the number of reject true positives, the applied significance threshold was informed by visual inspection of the power spectra that felt close to the acceptance/rejection cut-off. This approach returned 1106 oscillating stars. The central three radial orders of the power excess is then fitted by a sequence of Lorentzian profiles representing oscillation modes and parameterised by the frequency of the central radial mode and a large and small frequency separation (Kallinger et al. 2010, 2014). However, the fit to extract $\Delta\nu$ returned robust results only for a subset of the stars (583 stars).

COR: The method is the same as used for CoRoT or *Kepler* stars (Mosser & Appourchaux 2009). The large separation is detected first, from the autocorrelation of the time series computed as the Fourier spectrum of the filtered Fourier spectrum of the signal (EACF). A simple statistical test based on the H0 hypothesis is used to assess the significance of the $\Delta\nu$ detection from the value of the EACF. In case of positive detection, the other global seismic parameters are determined. A star is regarded to show solar-like oscillations if its $\Delta\nu$, FWHM of the smoothed power excess, mean height of the power excess at ν_{\max} , and height of the background at ν_{\max} all closely follow the empirically calibrated mean relations as a function of ν_{\max} (Mosser et al. 2012). For K2, a special treatment is applied to cope with the spacecraft thruster firing frequency. It consists in using the empirical scaling relations with stronger constraints when ν_{\max} is found to be near the firing frequency or its harmonics. Uncertainties are calibrated functions of the EACF parameter (see Mosser & Appourchaux 2009, for details). COR returned results for all stars thought to provide robust $\Delta\nu$ and ν_{\max} values (778 stars).

BHM uses a three-stage approach, described in detail in Elsworth (in prep.). To summarise: First, the white-noise-subtracted power spectrum is divided by a heavily smoothed version of the raw power spectrum, representing the noise profile, to create the signal-to-noise ratio (SNR) as function of frequency. The likelihood of each frequency bin representing just noise is then calculated according the H0 hypothesis. Next, we apply the H1 hypothesis to a series of overlapping frequency segments of gradually increasing central frequency along the SNR-spectrum. The width of each segment changes as function of its central frequency following the empirical oscillation power width- ν_{\max} relation from Mosser et al. (2012). The combination of H0 and H1 is used to form an odds ratio of there being oscillation signal in a given segment. If a segment shows detection of oscillation power, the next two stages provide estimates of ν_{\max} and $\Delta\nu$. This part of the method follows largely the OCT method described in Hekker et al. (2010), but with some extra selection criteria needed because of the short duration of the time series. For $\Delta\nu$, stringent

¹³ We refer to the pipelines with their commonly used nicknames.

tests are applied to mitigate against the measured $\Delta\nu$ being corrupted by the frequency spacing between the radial and octupole modes. These tests meant that for many of the stars only the ν_{\max} values is considered reliable. In total 1031 stars have a robust measurement of ν_{\max} , while only 198 have also a $\Delta\nu$ value.

A2Z+ is an improved version of the A2Z pipeline described by Mathur et al. (2010), but we refer to it in this paper simply as A2Z. It uses the same method as COR to determine a first estimate of $\Delta\nu$, and the frequency range where that signal is present, from which a collapsed echelle diagram is formed to determine the location of the radial modes. ν_{\max} is determined by fitting a Gaussian in top of the background to the power spectrum. The guess for granulation timescale used in the fit is based on the results from Mathur et al. (2011). For stars where the highest radial mode was statistically significant at the 99% level, $\Delta\nu$ is recomputed from the power spectrum of the power spectrum (PS2) where the dipole modes are masked out. Here, we use only the central orders of the spectrum centered on the highest radial mode. The number of radial orders used is typically four but depends slightly on the signal-to-noise ratio and ν_{\max} . The power spectrum and echelle diagram are used to visually verify the $\Delta\nu$ measurements, and only stars with convincing detections are kept. Finally, as a post-processing criteria, stars are kept only if the slope of a linear fit to the power spectrum in log-log space is steeper than -0.5. In order words, if the granulation signal is not clear the star is not expected to show clear oscillations either (and is most likely a dwarf or too faint giant with a white noise dominated spectrum). Uncertainties were computed with a weighted centroids method that depends on the frequency resolution in the PS2. Because we used the same number of orders around ν_{\max} for most stars, the relative uncertainties are generally very similar for the stars. A2Z returned ν_{\max} and $\Delta\nu$ results for 673 stars.

SYD: This pipeline is described in detail in Huber et al. (2009), and uses Monte-Carlo simulations to generate statistically perturbed spectra from which measurement uncertainties are estimated as described in Huber et al. (2011). The pipeline does not include a statistical assessment of whether oscillations are present in the data. Hence, to automate the selection of robust detections we impose a number of post processing criteria. First, stars are kept only if the power spectrum is steep enough to show the presence of granulation, using the same criteria as A2Z. Secondly, the correlation between an empirical average model spectrum and the slightly smoothed collapsed power spectrum of the central four orders need to be above a certain cut-off value (to ensure a clear mode pattern revealing $\Delta\nu$). The correlation process follow that of Stello et al. (2016a), and like CAN, the cut-off is informed by visual inspection of stars that are accepted versus rejected. Thirdly, the stars need to have a $\Delta\nu$ within 30% of the average expected $\Delta\nu$ from the $\Delta\nu$ - ν_{\max} relation of (Stello et al. 2009). This cut was chosen based on the natural spread seen among the high signal-to-noise *Kepler* red giant sample (Stello et al. 2013). Finally, stars need to have an oscillation amplitude within a factor of two of the average fiducial amplitude- ν_{\max} trend seen for spectroscopically confirmed red giants from Stello et al. (2015). SYD returned results for all stars thought to provide robust values for both $\Delta\nu$ and ν_{\max} (559 stars).

BAM: Like CAN, BAM uses a Bayesian MCMC scheme for fitting the background and the oscillation excess power hump in the frequency spectrum, and for estimation of the

TABLE 1
NUMBER OF RED GIANTS WITH DETECTED ν_{\max} AND COMPARISON WITH VISUAL INSPECTION.

Pipeline	CAN	COR	BHM	A2Z	SYD	BAM	Comb.
Total	1106	778	1031	673	559	951	1262
Yes	1017	745	980	638	537	905	1100
	% (92.0)	(95.8)	(95.1)	(94.8)	(96.1)	(95.2)	(87.2)
Maybe	67	28	36	26	17	34	110
	% (6.1)	(3.6)	(3.5)	(3.9)	(3.0)	(3.6)	(8.7)
No	22	5	15	9	5	12	52
	% (2.0)	(0.6)	(1.5)	(1.3)	(0.9)	(1.3)	(4.1)

The ‘Total’ numbers are split into the three visual classification categories shown both as absolute numbers and in percent for each pipeline. Due to rounding, the percentages do not necessarily add to exactly 100%. ‘Comb.’ refers to stars with at least one pipeline detection.

TABLE 2
NUMBER OF RED GIANTS WITH DETECTED $\Delta\nu$.

Pipeline	CAN	COR	BHM	A2Z	SYD	BAM	Comb.
Total	583	778	198	673	559	759	1184

‘Comb.’ refers to stars with at least one pipeline detection.

measurement uncertainties (Zinn et al. in prep.). It first fits a two-component noise background (plus white noise) whose resulting parameters are subsequently used as priors on a fit to the oscillation excess, modeled as a Gaussian with amplitude, width, and center (ν_{\max}) as free parameters. One set of priors are calculated from empirical correlations between the background parameters and ν_{\max} ; another prior is placed on the timescale ratio between the two background components; and a final set of priors link ν_{\max} to the Gaussian amplitude and width. These priors are then used to derive the (total prior) probability of finding the measured value of each fitted parameter. After fitting the model (of noise plus excess) to the power spectrum, BAM selects a star as an oscillator if: 1) the signal-to-background ratio at ν_{\max} is greater than 3.0, and 2) the total prior probability is within the 4-sigma confidence interval. Subsequently, $\Delta\nu$ is determined by a least-squares fit to the folded spectrum using the $4\Delta\nu$ -wide ν_{\max} -centered section of the spectrum with $\Delta\nu$ as the folding frequency. The folded radial, dipole, and quadrupole mode regions are each modeled with a Lorentzian function. The uncertainty in $\Delta\nu$ is estimated as the quadrature sum of the uncertainties on the mode widths and locations. $\Delta\nu$ is returned for stars only if the probability of $\Delta\nu$ and the mode visibilities are within 4σ of their expected values based on priors. BAM returned ν_{\max} for 951 stars and $\Delta\nu$ for 759 stars.

Some of the pipelines used here have previously been compared on the basis of *Kepler* data. Although they have improved since, and changes has been made to accommodate K2-specific issues, we refer the reader to such comparison papers for additional reading (Hekker et al. 2011b, 2012).

4. SEISMIC RESULTS

In Table 1 we list the total number of stars for which each pipeline detected the presence of oscillations, meaning at least a measurement of ν_{\max} . When combined, we found 1262 unique stars with at least one pipeline reporting detection. In Table 2 we list the total number of stars for which the pipelines also detected $\Delta\nu$.

The $\Delta\nu$ and ν_{\max} values from each pipeline are listed in Table 3. All stars with no detection of oscillations, are listed in Table 4 by their EPIC ID, Kp , and $\log g$ -range classification probability from stellar population modeling using *Galaxia*. They are a source of mostly dwarfs with a well characterised selection function (Section 2).

In addition to the following verification and completeness analyses, we show a series of figures in the Appendix comparing the results from the individual pipelines to aid the use of this rich and versatile data set. The figures highlight statistical properties of the results including the natural biases between pipelines arising from the fact that each pipeline measures and hence defines the seismic observables in slightly different ways. Users for which the magnitude of these biases are important for their science are strongly encouraged to familiarise themselves with the specific methods adopted by the pipelines and their comparisons (see references in Sect. 3.1).

4.1. Visual verification

We visually inspected power spectra for all 1262 pipeline-detected giants, and assigned them to one of three categories ‘Yes’, ‘Maybe’, or ‘No’, according to whether they showed oscillations and/or granulation. This is obviously a subjective approach, which in a sense takes a continuum of probabilities of a star showing oscillations and puts that into three bins. However, we did it such that ‘Yes’ meant we felt confident the star oscillated, while ‘No’ meant we were confident it did not oscillate below the Nyquist frequency. Figure 2 shows a sample representative of low (left panels), medium (centre panels), and high (right panels) ν_{\max} detections (by the pipelines). For each ν_{\max} case we show the resulting three different visual detection categories; except for the low ν_{\max} case, where there were no stars categorised as ‘No’ detections, for which we instead show a ‘Maybe’ case that straddle the No category.

To test the subjectivity of our visual inspection, we had two people look through the power spectra independently. Cross checking their results showed not a single case where one person said ‘No’ and the other said ‘Yes’, and there were only five borderline cases between neighboring categories, where one said ‘Yes’ or ‘No’ and the other said ‘Maybe’. We therefore regard the result of the visual inspection as highly robust. A similar exercise had been implemented by Stello et al. (2013), also showing consistency between three independent people. We include the result of the visual detection verification in Table 3 and summarise how each pipeline performs relative to our visual inspection in Table 1 (in pure counts and percent). It is worth noting that despite the larger number of stars returned by CAN, BHM, and BAM, those samples seem to be of similar quality as the rest (high ‘Yes’ and low ‘No’ fractions).

Of the 1262 giants detected by at least one pipeline, we found 1100 in the ‘Yes’ category, 110 were assigned as ‘Maybe’, and 52 ‘No’ detections. If we assume the ‘Maybe’ cases are all genuinely oscillating giants, just with low S/N ratios or with ν_{\max} outside the 10-270 μHz range, this would suggest we have up to ~ 1210 detections.

To further double check that the confirmed detections were in line in terms of their ν_{\max} values, we compared pipeline values with visual values. The latter was found by manually placing (and mouse-clicking) a cursor on interactive plots of power spectra at the location of ν_{\max} . The intrinsic uncertainty in performing this manual ν_{\max} localisation, of up to 30%, meant we could safely use them to identify clear out-

TABLE 3
SEISMIC RESULTS AND VISUAL DETECTION VERIFICATION OF 1262 GIANTS DETECTED BY AT LEAST ONE PIPELINE. ‘Y’=CLEAR DETECTION; ‘M’=MAYBE DETECTION; ‘N’=NO DETECTION; ‘O’=CLEAR DETECTION BUT ν_{\max} OFF. ALL FREQUENCIES AND THEIR UNCERTAINTIES ARE LISTED IN μHz .

EPIC ID	Detec.	CAN	COR	BHM	A2Z	SYD	BAM																		
		$\Delta\nu$	ν_{\max}	$\Delta\nu$	ν_{\max}	$\Delta\nu$	ν_{\max}																		
201121245	Y	15.977	0.029	198.113	2.838	14.887	0.174	202.510	4.180	16.100	0.269	187.286	3.391	0.000	0.000	16.046	0.056	199.530	2.534	0.000	0.000	0.000	0.000		
201126368	M	0.000	0.000	0.000	0.000	4.211	0.075	47.470	1.240	0.000	0.000	0.000	0.000	0.000	0.000	0.000	0.000	0.000	0.000	0.000	0.000	4.579	0.046	42.966	0.966
201126489	Y	17.174	0.034	226.041	3.462	0.000	0.000	0.000	0.000	16.851	0.879	223.491	5.228	17.200	0.108	226.274	15.172	17.160	0.035	224.334	3.154	17.003	0.026	224.423	3.129
...

full table is available electronically
Stars that do not follow the K2 GAP target selection (Sect 2) are listed with their EPIC IDs made negative.

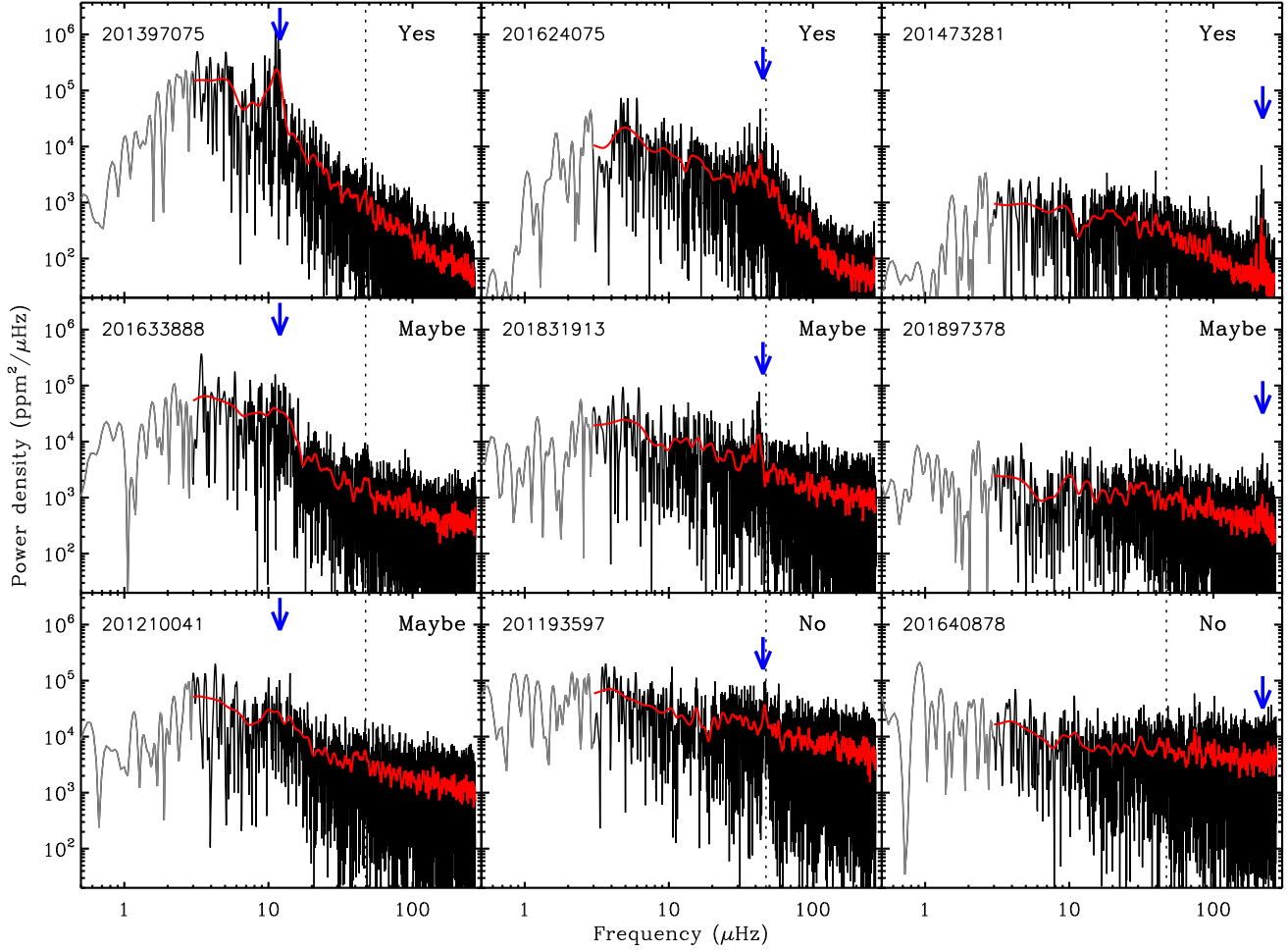


FIG. 2.— Example power spectra for three representative ν_{\max} values (left panels: $\nu_{\max} \sim 10 \mu\text{Hz}$; centre panels: $\nu_{\max} \sim 45 \mu\text{Hz}$; right panels: $\nu_{\max} \sim 220 \mu\text{Hz}$), and three different visual verification categories (top panels=Yes; middle panels=Maybe; bottom panels=No). There was no ‘No’-category stars with a low ν_{\max} measurement by the pipelines, hence the bottom left panel shows a Maybe case. The raw spectra are shown in black and the part affected by the high-pass filtering in grey. Heavily smoothed spectra are shown in red. Approximate ν_{\max} values detected by the pipelines is indicated by the blue arrows, and the dotted vertical lines shows the spacecraft thruster firing frequency. Each star is indicated by their EPIC ID (Huber et al. 2016).

TABLE 4

LIST OF STARS WITHOUT SEISMIC DETECTION (ALMOST ALL DWARFS). PROBABILITIES ARE DIVIDED INTO FOUR RANGES OF $\log g$: $\log g < 1.9$, $1.9 < \log g < 3.2$, $3.2 < \log g < 4.2$, $\log g > 4.2$ (SEE SECT. 4).

EPIC ID	Kp [mag]	Probability [%]			
		$P_{<1.9}$	$P_{1.9-3.2}$	$P_{3.2-4.2}$	$P_{>4.2}$
201122454	13.85	4	1	0	*95
201123619	15.21	2	0	0	98
201124136	12.24	16	19	2	63
...

* Due to rounding errors, the printed probabilities do not necessarily add to exactly 100%.
(full table is available electronically)

liers. It was encouraging to see only a handful of pipeline results were indicated as outliers.

4.2. Ensemble verification

One way to check that the $\Delta\nu$ and ν_{\max} measurements originate from oscillations and not from spurious humps of excess power is to verify that the amplitude, or some sort of

similar measure of mode oscillation strength, show a correlation with ν_{\max} as expected from scaling relations (e.g. Stello et al. 2007), and empirically demonstrated for large samples of giants (e.g. Mosser et al. 2010; Huber et al. 2010). In Figure 3 we show mode strength versus ν_{\max} for the pipelines that return both quantities. All panels show correlations indicative of detections due to oscillations. We also indicate the visual verification results by different colored symbols. It is reassuring to see that the ‘No’ detections (red open symbols) fall predominantly in the narrow frequency ranges around the spacecraft’s thruster firing frequency and its harmonics or very close to the Nyquist frequency. Due to an improvement in the spacecraft altitude control since campaign 3, we expect the thruster firing will have negligible impact on the data for later campaigns as evidenced by the clean C5-based data in Stello et al. (2016b). The ‘Maybe’ category is spread out more (magenta filled symbols), but often at extreme frequencies pushing the limit of what can be measured with the length and sampling of the K2 data. Or they are near the artifacts from thruster firings; although a significant fraction are between 20 and 30 μHz which are probably helium-core burning stars or possibly artifacts at half the thruster firing frequency. These results show that the visual inspection provides

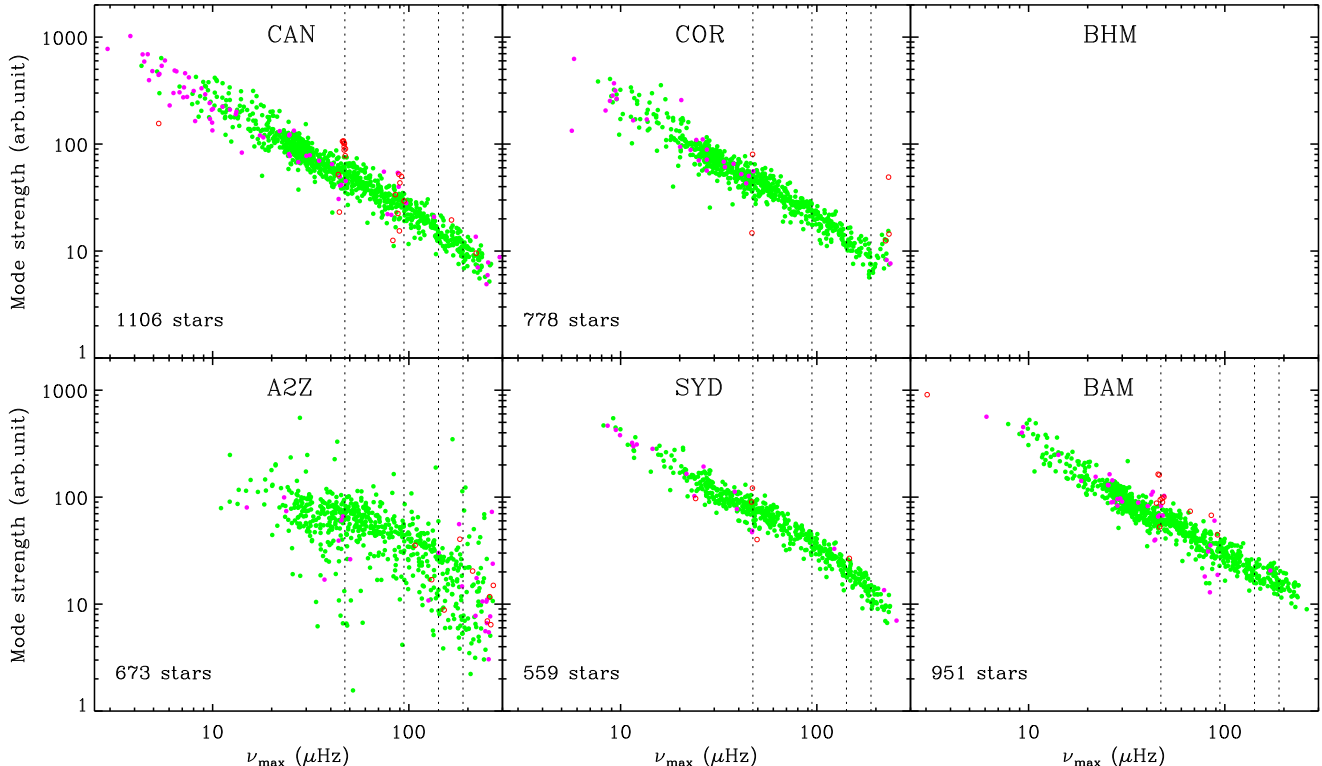


FIG. 3.— Mode strength versus ν_{\max} from each pipeline. Mode strength is synonym for either oscillation amplitude or some other measure of the oscillation excess power (BHM did not return such values). The K2 thruster firing frequency and its first few harmonics are shown by dotted lines. Green filled: ‘Yes’ detections, Magenta filled: ‘Maybe’ detections, and Red open: ‘No’ detections by visual inspection.

valuable complementary information, which suggests that the pipelines only struggle in a limited range and mostly extreme ends of the parameter space.

To further investigate whether the seismic measurements agree with expectations, we show the $\Delta\nu$ - ν_{\max} relation in Figure 4, which is expected to be relatively tight both from scaling relations (Stello et al. 2009) and as demonstrated for large samples of giants (e.g. Hekker et al. 2009; Huber et al. 2010). From *Kepler* data we generally do not see stars outside the $\pm 20\%$ range around the mean $\Delta\nu$ - ν_{\max} relation (solid lines), which roughly encompasses a mass spread of 0.5 - $2.5M_{\odot}$.

5. COMPLETENESS OF SEISMIC SAMPLE

In the following we investigate to what extent our resulting sample of oscillating giants is affected by detection bias. Unlike Stello et al. (2015) we do not have prior spectroscopic knowledge of the evolutionary state of our stars to guide this analysis. For a given non-detection we can therefore not be certain if it is outside the detectable frequency range or if it is just a very low S/N case. However, we have a much larger set of stars than in Stello et al. (2015), which should enable us to make inference on the presence of likely detection biases by comparing our samples of $\Delta\nu$ and ν_{\max} detections, and in turn compare the latter sample with a synthesized population. The obvious caveat with the synthesized population will be its model dependency. But as long as the model is not grossly inaccurate we can reasonably assume only small detection biases could remain unnoticed.

5.1. Completeness of $\Delta\nu$ sample

Comparing the number of stars between Figure 3 and 4 plotted in each panel, illustrates that more stars show evidence of oscillation excess power (a ν_{\max} measurement) than a clear frequency pattern from which $\Delta\nu$ can be determined (see also Tables 1 and 2). This is an inevitable consequence of the length of the time series, which is not long enough to fully resolve the mode patterns in some of the stars. In Figure 5 we show the histogram of stars with a visually verified ν_{\max} measurement (green), compared to those where we also have a $\Delta\nu$ measurement (blue). It is evident that the problem of identifying $\Delta\nu$, affects the helium-core burning stars the most, particularly stars with ν_{\max} around $30\mu\text{Hz}$. This arises because they show more complex frequency spectra, and mode power is spread into more frequency bins, which are therefore each of lower amplitude, resulting in less clear mode patterns. Based on Figure 5 we conclude the sample of stars with both $\Delta\nu$ and ν_{\max} measurements is biased at least for helium-core burning stars. It is not clear if that applies only to the helium-core burning stars that have $\nu_{\max} \sim 30\mu\text{Hz}$. The $\Delta\nu$ detection bias is more severe for some pipelines where we see a clear lack of stars in the blue curve compared to the green curve (e.g. CAN), potentially affecting all stars with $\nu_{\max} \lesssim 50\mu\text{Hz}$. Looking at Hekker et al. (2011a) (their Figure 2) it seems that for 50-100 day *Kepler* time series, which brackets the 80-day K2 C1 series, there is a deficit of stars with $\Delta\nu$ in the range 3 - $5\mu\text{Hz}$ (equivalent to $\nu_{\max} \sim 30\mu\text{Hz}$) relative to the expected smooth decrease in detections for decreasing $\Delta\nu$ (or ν_{\max}). This is in qualitative agreement with what we see here for K2. We therefore recommend that the $\Delta\nu$ detection bias for the potentially affected stars ($\nu_{\max} \lesssim 50\mu\text{Hz}$) be quantified specifically for K2 using the same pipelines as presented here before the $\Delta\nu$ re-

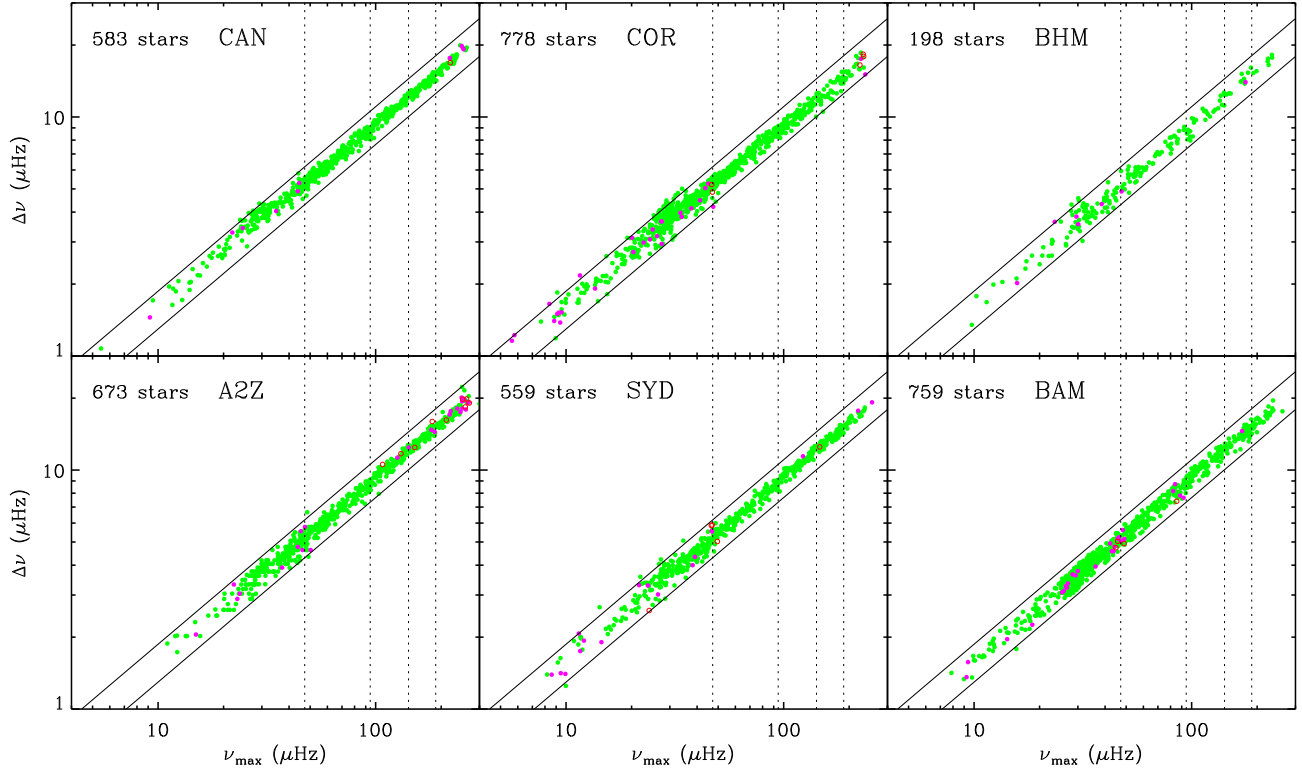


FIG. 4.— $\Delta\nu$ - ν_{\max} relation from each pipeline. The K2 thruster firing frequency and its harmonics are shown by dotted lines. To guide the eye, black lines show $\pm 20\%$ brackets from the $\Delta\nu$ - ν_{\max} relation by Stello et al. (2009) outside which one would normally not find robust detections of high S/N (e.g. from 4-yr *Kepler* data). Green filled: ‘Yes’ detections, Magenta filled: ‘Maybe’ detections, and Red open: ‘No’ detections by visual inspection.

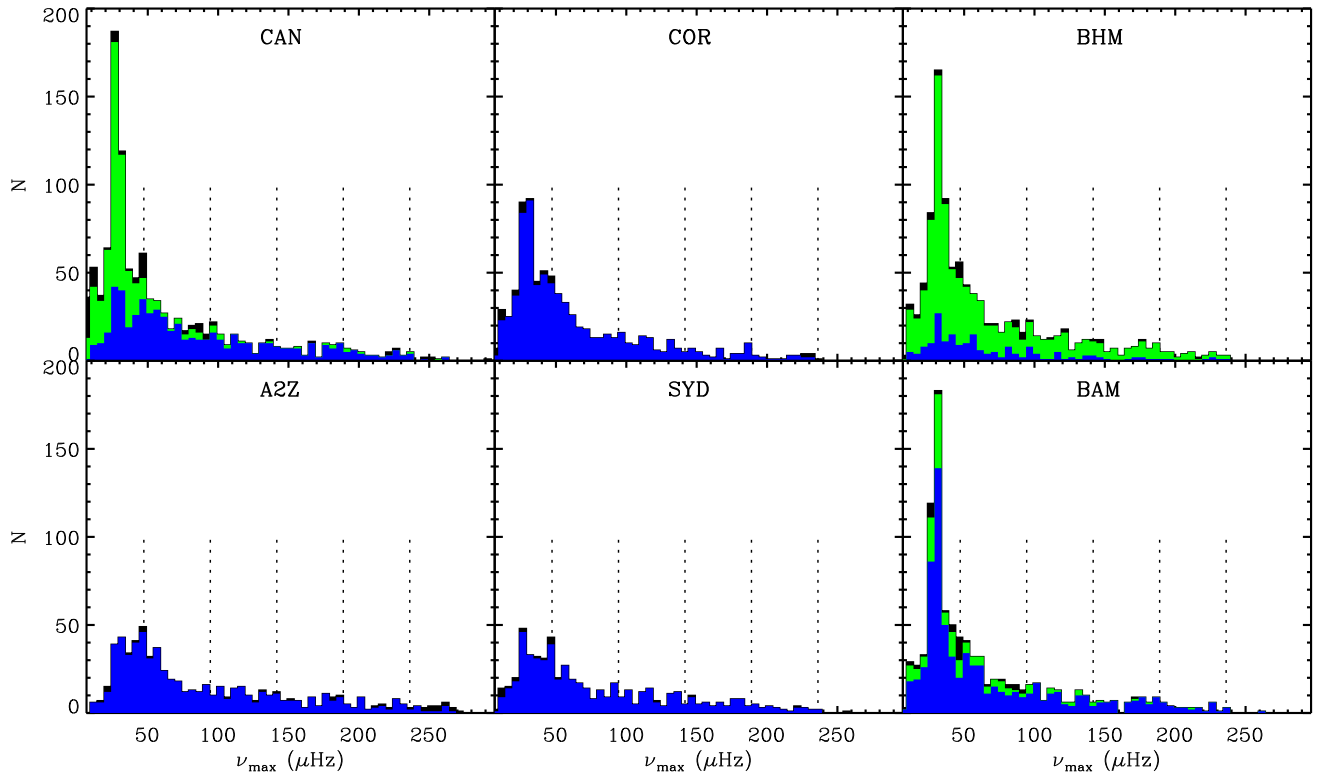


FIG. 5.— Distribution of ν_{\max} for detected red giants. Black shows all stars with a measured ν_{\max} value, while green shows only the visually verified ‘Yes’ detections. Blue represent the verified detections for which $\Delta\nu$ is also measured (equal to green for COR, A2Z, and SYD).

sults of these stars are used for population studies. However, the reported $\Delta\nu$ could of course still be used safely for other purposes (or indeed for population studies restricted to stars in the unaffected ν_{\max} range (Figure 5).

5.2. Completeness of ν_{\max} sample

5.2.1. Individual pipeline results

Here, we will compare our number of detected giants with what one would expect from synthesizing our target sample. We note that while the total number of detected giants is up to 1210, they were found among all 8,630 observed stars in the K2 GAP list, rather than only the 8,385 that follow the K2 GAP selection (Section 2). Hence, about 30 of the detected giants are serendipitous from other K2 proposals, which should be subtracted before comparing with a synthesized sample¹⁴. We use the Galaxy synthesis tool, *Galaxia* to synthesize our target sample of 8,385 stars by imposing the selection described in Section 2, and the ν_{\max} detection range of 10-270 μHz . This results in an initial ~ 1650 expected giants (within Poisson error) in the detectable ν_{\max} range, which is significantly larger than the number of giants actually detected. Hence, we want to investigate whether there might be any significant biases with respect to signal and/or noise. The signal is the oscillation amplitude for which ν_{\max} is a good proxy (Fig. 3), while the noise can be approximated by brightness, Kp . In Figure 6 we therefore show ν_{\max} and Kp for all visually inspected detections (green, magenta, and red symbols). The grey dots in the background show the synthesis population of 1650 expected giants. It is clear from this comparison that we can not detect oscillations in stars in the upper right corner, which are the faintest (more noisy), and the least evolved stars (highest ν_{\max} and hence lowest intrinsic oscillation amplitudes).

To assess if this apparent ‘lack’ of faint low luminosity red giants is expected, we need to take the oscillation detectability into account. We derive the detectability following the formulation by Chaplin et al. (2011). The stellar properties are given as part of the output from *Galaxia*, from which the oscillation and granulation signal is predicted. Different to Chaplin et al. (2011), we use the more up-to-date relation for oscillation amplitude by Stello et al. (2011), which is empirically calibrated by open cluster red giants. We also need to re-calibrate the noise estimates compared to the *Kepler* results (Jenkins et al. 2010) adopted by Chaplin et al. (2011) to incorporate the K2-specific noise properties. To illustrate the K2-*Kepler* noise difference, we show in Figure 7 the measured scatter in the time series for all stars in our sample (black dots). For comparison we show the noise floor of the equivalent *Kepler* time series scatter from Jenkins et al. (2010) (dotted red curve), which matches the K2 noise floor quite well (grey dotted curve) when shifted up be a factor of two. However, this noise floor is clearly a lower limit even for photon noise dominated stars ($Kp \gtrsim 14$), which for the vast majority show a scatter that ranges a factor of four. We therefore adopt a larger and more representative noise level for K2 of three times the *Kepler* level (solid red curve).

Now, taking our derived detectability into account, we expect to detect oscillations in only ~ 1420 of the synthesis sample (Figure 6, black dots). This synthesis sub sample shows the same lack of stars as our observations in the top right corner in the Figure 6 main panels. For added clarity

we also show histograms of the observed and synthesis distributions as function of ν_{\max} and Kp . The Kp distributions demonstrate a drop in stars occurs beyond $Kp = 12.5$ - 12.7 (green curve), which is similar to what is expected from the *Galaxia* distribution peaking at $Kp = 12.7 - 13.0$ (black curve). There seem to be a tendency for all pipelines to claim detections where no detection was verified by the visual inspection for stars fainter than $Kp \sim 15$ (red open symbols). We therefore caution using these seismic results of stars fainter than $Kp \simeq 14.5$ for population studies due to potential completeness issues in the current sample of results. However, we note that the lack of luminous faint ($Kp > 15$) giants in our C1 sample prevents us from reaching definitive conclusions about detection bias towards the faint end.

5.2.2. Combined pipeline results

Now we turn to the combined set of results, and show the sample distribution in ν_{\max} - Kp space in Figure 8. Here we acknowledge that different pipelines have different strengths and by compiling all the stars for which at least one pipeline detected oscillations, we are more likely to obtain as many stars as possible in our sample. Hence, our sample will be more likely to contain, as closely as possible to, all detectable oscillating stars. For this part of our investigation we adopted ν_{\max} values first sourced from CAN, then we added those from A2Z not already in the CAN sample, then BHM, SYD, COR, and finally BAM, following the order of the pipeline with the most to least unique detections. By construction, not all stars in the compiled list have a ν_{\max} value from the same pipeline. However, for the purpose of investigating the completeness of the population as a whole, the relatively small ν_{\max} biases between different pipelines plays no important role (Appendix, Figures 17, 18).

To use the sample for population studies one needs to take into account that we can not detect stars above the fiducial dotted curve, expressed by $\nu_{\max, \text{detect}} < 2.6 \times 10^6 \cdot 2^{-Kp} \mu\text{Hz}$. We note that the curve seems to have a slightly steeper dependence on Kp than predicted (see black dots). The predicted dependence is close to $\propto 2^{-0.4Kp}$ as expected from the photon noise limit, and we attribute the steeper observed dependence to the fact that our adopted noise estimate becomes increasingly underestimated towards fainter stars; as opposed to bright stars where the photon noise plays no significant role in the detectability. In order words, our simple noise prescription does not take full account of the gradual transition between the two noise regimes and the intrinsic spread in the noise from star to star. It is therefore also difficult to make an accurate model prediction of the absolute number of expected detections. Changing the adopted noise level by about 30%, changes the number of expected detections by about 100 (with larger noise resulting in fewer expected detections).

From the distributions shown as histograms of different parts of the ν_{\max} - Kp parameter space we see that the discrepancy between observed and predicted number of stars seems to be more pronounced for $\nu_{\max} \lesssim 40 \mu\text{Hz}$, which affects many helium-core burning stars. Here it shows about a 30% difference (Figure 8, right panels). This difference could be due to both observation bias and errors in the Galactic model prediction including predictions of oscillation amplitude and noise. While observational detection bias of ν_{\max} would not be unexpected for the faintest stars, it is surprising to see the quite pronounced discrepancy for the bright stars. There were no strong indications of such pronounced discrepancies for the *Kepler* red giant sample based on two years of data

¹⁴ In Table 3 we have marked the stars that do not following the K2 GAP selection

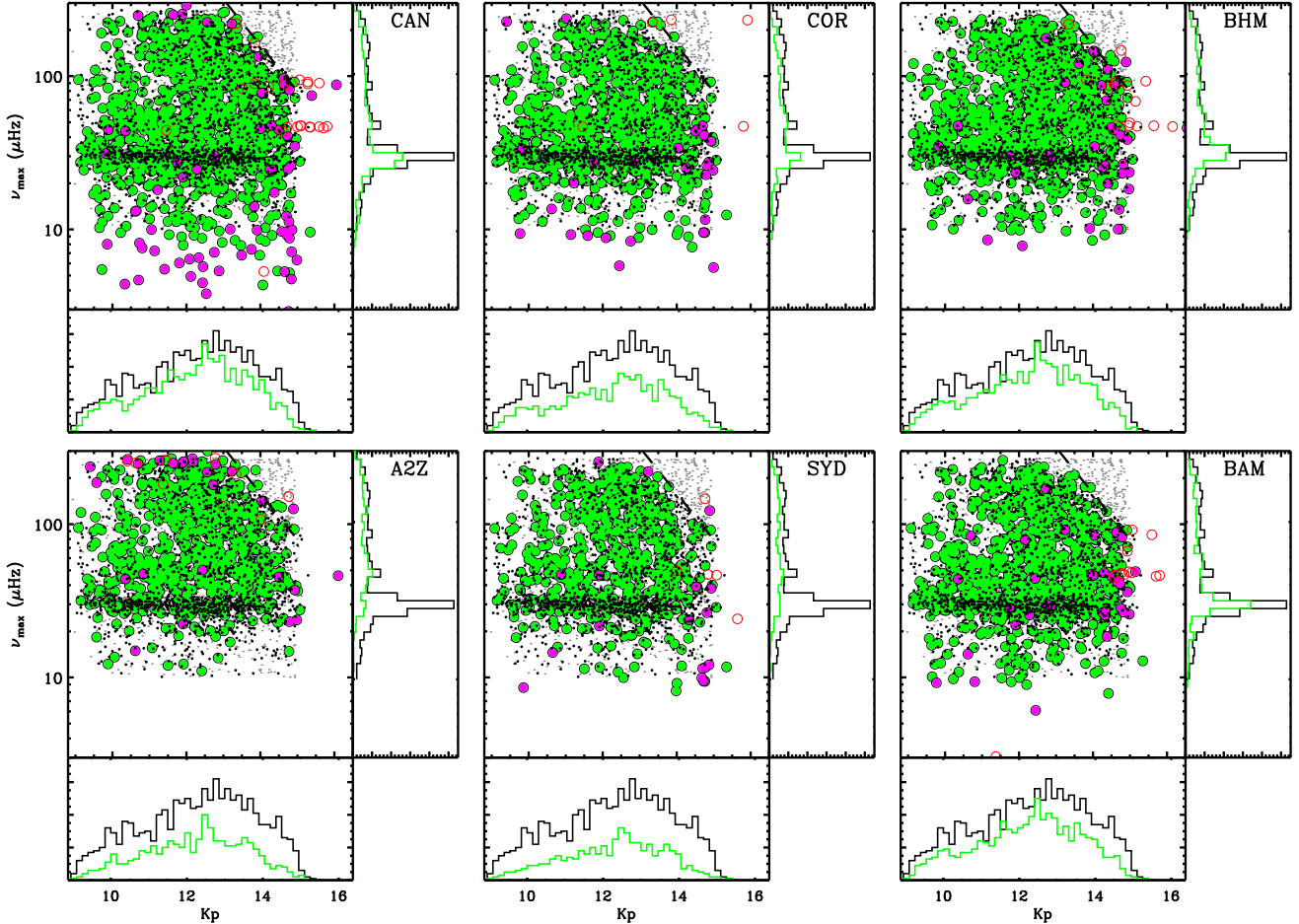


FIG. 6.— ν_{\max} versus Kp of seismic sample from each pipeline. Green filled symbols shows only stars verified visually as clear detections, while magenta filled symbols are maybe detections, and red open symbols are non-detections. Small grey dots show the *Galaxia*-synthesized population. Black dots show only those *Galaxia* stars with more than 95% probability of detection according to the Chaplin et al. (2011) formulation. The dashed line shows a fiducial detection limit (the same line is used in all panels for comparison), such that oscillations in stars above the line can not be detected ($\nu_{\max, \text{detect}} < 2.6 \times 10^6 \cdot 2^{-Kp}$ μHz). The distributions of the green symbols and black dots are shown as histograms in ν_{\max} and Kp .

(Sharma et al. 2016). However, due to the unknown selection function of the *Kepler* giants direct comparisons can not be made with what we see here for the K2 C1 sample. In the bottom histogram we also do not see any strong dependence on Kp for the difference between observed and predicted star counts, except perhaps a small tendency of relatively fewer observed stars fainter than $Kp \sim 13.5 - 14.0$, mostly arising from the before-mentioned slight difference in observed and predicted bias around the sloping dashed line (faint low luminosity stars). Also in this histogram, we see that the star counts agree quite well for $\nu_{\max} > 40$ μHz (dotted curves) in agreement with the above discussion.

In summary, we see an expected (and largely predicted) detection bias for faint low luminosity red giant branch stars and an apparent, but still not fully understood, difference between observed and predicted star counts for red clump stars across all magnitudes.

5.3. Comparison to EPIC classifications

Another source to investigate completeness are the stellar classifications provided in the Ecliptic Plane Input Catalog (Huber et al. 2016). While the EPIC uses *Galaxia* models for stellar parameter inference, the classifications are based on observational data such as reduced proper motions, col-

ors, and spectroscopy, hence providing a more empirical test of the completeness of the seismic sample. Based on simulations and comparisons to the *Kepler* Stellar Properties Catalog (Huber et al. 2014; Mathur et al. 2016), the dwarf/giant misclassification fraction in the EPIC is expected to be $\sim 5\%$.

Of the 1262 stars with a ν_{\max} value reported by at least one pipeline, all but one are classified in the EPIC. Of these, $\sim 9\%$ are classified as dwarfs in the EPIC ($\log g > 4$) and $\sim 2\%$ are classified as cool dwarfs ($\log g > 4$, $T_{\text{eff}} < 4000$ K). We expect that the hotter dwarfs ($T_{\text{eff}} > 4000$ K) are significantly affected by classification errors in the EPIC, and hence account for most of the 5% misclassification fraction mentioned above. Inspection of a 2MASS color-color diagram showed that at least half of the dwarfs with $T_{\text{eff}} < 4000$ K indeed have colors consistent with cool dwarfs. We therefore conclude that the fraction of seismic stars in our sample which are in fact dwarfs (with the seismic signal introduced e.g. by blended giants) is $\sim 2\%$.

Using the EPIC to estimate the number of missing seismic detections is more difficult, since the typical EPIC $\log g$ uncertainties on the RGB can be as high as 0.3 dex. Nevertheless, the fraction of C1 GAP targets which are classified with $3.2 < \log g < 1.9$ and $\nu_{\max} < 2.6 \times 10^6 \cdot 2^{-Kp}$ in the EPIC

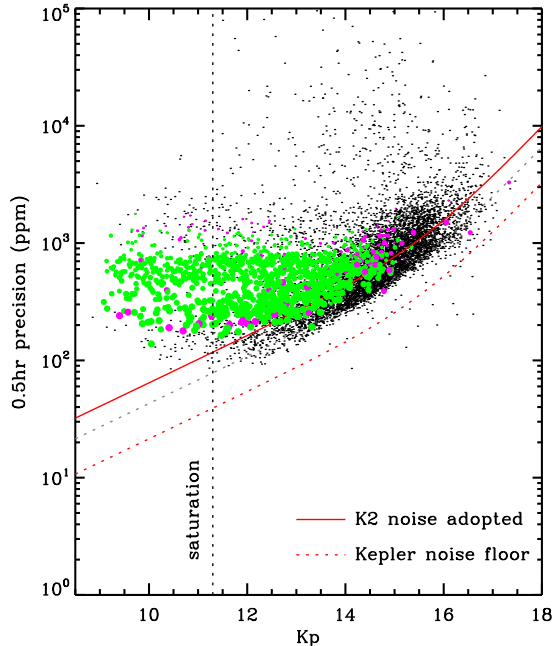


FIG. 7.— Time series scatter (standard deviation) versus Kp of all K2 GAP targets (black dots). Green filled symbols shows stars verified visually as clear detections, while magenta filled symbols are maybe detections. Symbol size scales with ν_{\max} . Vertical dotted line indicates the saturation limit. The dotted red curve shows the *Kepler* noise floor from Jenkins et al. (2010). The grey dotted line is shifted up by a factor of two. The red solid curve illustrates our adopted K2 noise, obtained by raising the *Kepler* noise floor by a factor of three.

is $\sim 14\%$ (corresponding to ~ 1200 stars), which is close to the observed fraction. This supports the conclusions based on the *Galaxia* models that the seismic sample is near complete.

6. CONCLUSION AND FUTURE OUTLOOK

We have analysed all (8,630) stars from the target list of the K2 Galactic Archaeology Program, and report the detection of oscillations in about 1200 of them; all red giants with $1.9 \lesssim \log g \lesssim 3.2$. As a serendipitous, but valuable by-product of this analysis, we identify a set of roughly 7500 dwarfs ideally suited for exoplanet galactic exoplanet occurrence rate studies.

- As expected for the giants, we find that $\Delta\nu$ can not be determined robustly for all the helium-core burning stars despite them showing oscillations, with a robust measurements of ν_{\max} .
- However, somewhat unexpectedly we see a discrepancy in star counts between a galactic synthesis-model prediction and the lower number of observed giants with a detection of $\nu_{\max} \lesssim 40 \mu\text{Hz}$, hence affecting many of the helium-core burning stars. Current evidence does not allow us to conclude to what degree this is caused by model error, including our ability to estimate oscillation amplitude and noise in the data, or by seismic detection bias against helium-core burning giants. This discrepancy clearly needs further investigation in future.

- One would go some way towards addressing this issue by applying the current seismic analysis pipelines on *Kepler* data ‘degraded’ to K2 quality; meaning short time series and higher noise levels, although not all K2-specific noise properties are straightforward to simulate with *Kepler* data.
- Performing a visual inspection along the lines what we show here, but for a large randomly selected set of stars, irrespective of pipeline detection or not, could indicate how many oscillating giants that were completely missed by any of the automated pipeline algorithms.
- It would further help to look at different galactic population synthesis tools (e.g. TRILEGAL Girardi et al. 2005) and to probe into different directions of the Galaxy using data from subsequent K2 campaigns, to investigate issues with the galactic model predictions. Already published results from later campaigns also indicate reduced effects from spacecraft thruster firings, making a comparison with *Kepler* data more informative.
- In addition, spectroscopic $\log g$ values from large unbiased samples of K2 GAP targets will provide an important independent comparison to reveal detection biases in the seismic sample.

- Despite the known biases, it currently appears that the sample of oscillating giants with $40 \lesssim \nu_{\max}/\mu\text{Hz} \lesssim 270$ and $\nu_{\max} < 2.6 \times 10^6 \cdot 2^{-Kp} \mu\text{Hz}$ (Figure 5, 8), provide a set of stars with little or no detection bias, especially if only ν_{\max} is used (for example in combination with *Gaia* parallaxes).
- We note that the C1 data does not suitably inform about detection bias towards luminous giants fainter than about $Kp \simeq 14.5$.
- Finally, if users do not take our visual detection confirmation into account, we suggest to disregard all stars with ν_{\max} within a few μHz of the thruster firing frequency if an unbiased set of stars is required from the C1 seismic data reported here.

The K2 Galactic Archaeology Program is supported by the National Aeronautics and Space Administration under Grant NNX16AJ17G issued through the K2 Guest Observer Program. D.S is the recipient of an Australian Research Council Future Fellowship (project number FT1400147). S.M. acknowledges support from NASA grant NNX12AE167 and NNX16AJ17G. D.H. acknowledges support by the Australian Research Council’s Discovery Projects funding scheme (project number DE140101364) and support by the National Aeronautics and Space Administration under Grant NNX14AB92G issued through the Kepler Participating Scientist Program.

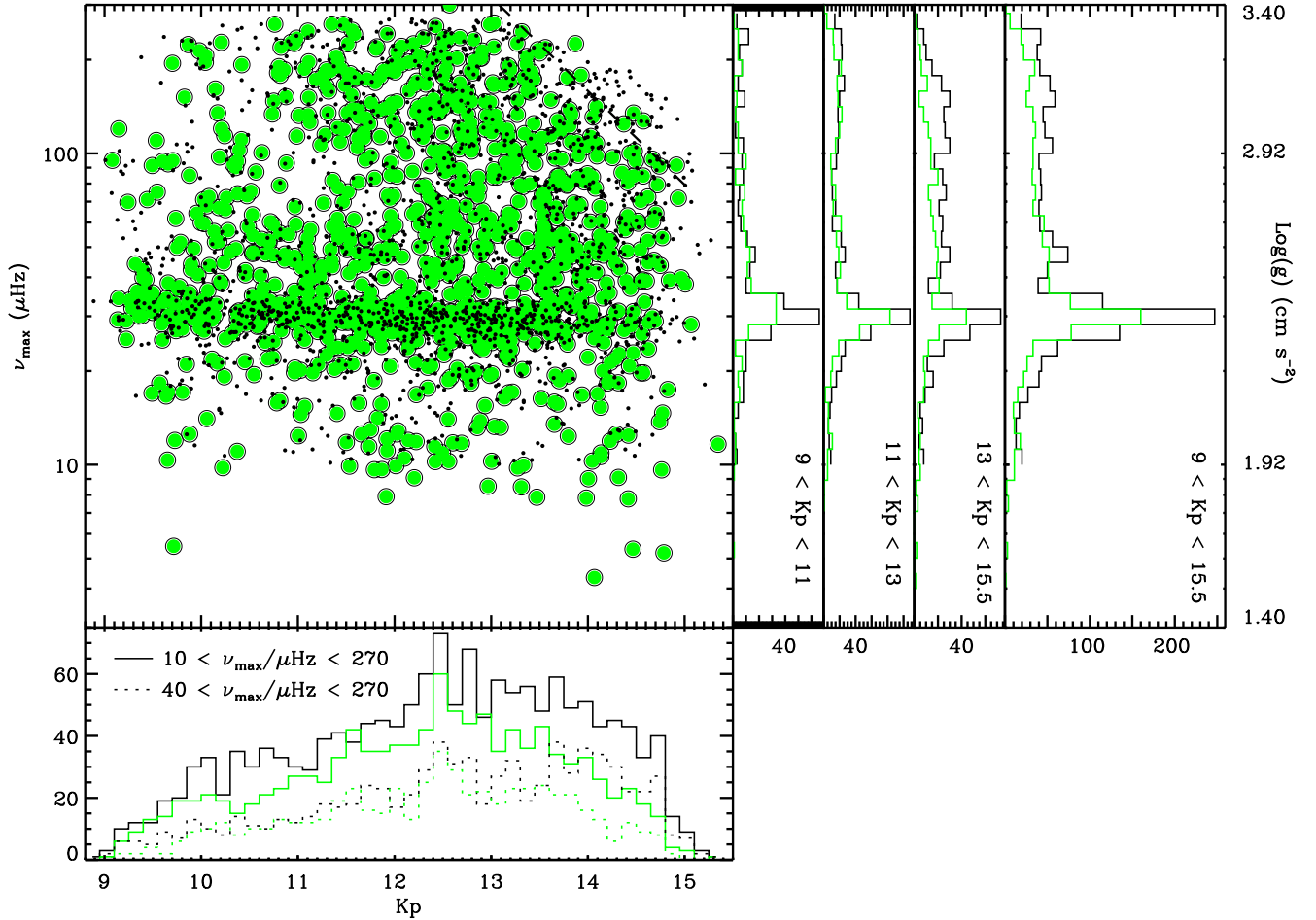


FIG. 8.— ν_{\max} versus Kp of combined seismic sample from all pipelines. The axis on the far right shows the approximate $\log g$ range. Green filled symbols/lines show only stars verified visually as clear detections. Black symbols/lines show the *Galaxia*-synthesized population that have more than 95% probability of detection according to the Chaplin et al. (2011) formulation. The dashed line in the main panel shows a fiducial detection limit ($\nu_{\max, \text{detect}} < 2.6 \times 10^6 \cdot 2^{-Kp} \mu\text{Hz}$), beyond which the signal-to-noise ratio is too low. The distributions of the green symbols and black dots are shown as histograms in ν_{\max} for different magnitude ranges and in Kp for different ν_{\max} ranges.

APPENDIX

This appendix is used to show some of the statistical aspects of the pipelines including biases between pipelines, which are a result of the different definitions of, and hence methods used to measure, $\Delta\nu$ and ν_{\max} . We refer the reader to previous comparisons by Hekker et al. (2011a, 2012) that included some of the pipelines used here, though somewhat earlier and modified versions relative to what is presented here.

We first show results for $\Delta\nu$. In Figure 9 we show the relative uncertainty in $\Delta\nu$ reported by each pipeline. The different methods for deriving uncertainties are clearly reflected in the different distributions of the relative uncertainties (see Section 3.1). In comparison Figure 10 shows the scatter between the pipelines for stars in common. Systematic pipeline-to-pipeline offsets in $\Delta\nu$ are illustrated in Figures 11 and 12, where the reference value is that from CAN, and in Figures 13 and 14, where the reference value is the mean across all pipelines.

Now we turn to the ν_{\max} measurements. In Figure 15 we show the relative uncertainty in ν_{\max} reported by each pipeline. Like in the case of $\Delta\nu$, here we also see clear differences in the distributions of the relative uncertainties. In comparison Figure 16 shows the scatter between the pipelines for stars in common. Pipeline-to-pipeline offsets in ν_{\max} are illustrated in Figures 17 and 18, where CAN is the reference value, and in Figures 19 and 20, where the reference is the mean across all pipelines.

REFERENCES

- Burke, C. J., et al. 2015, *ApJ*, 809, 8
 Chaplin, W. J., & Miglio, A. 2013, *ARA&A*, 51, 353
 Chaplin, W. J., et al. 2011, *Science*, 332, 213
 De Silva, G. M., et al. 2015, *MNRAS*, 449, 2604
 Girardi, L., Groenewegen, M. A. T., Hatziminaoglou, E., & da Costa, L. 2005, *A&A*, 436, 895
 Hekker, S., et al. 2009, *A&A*, 506, 465
 —. 2010, *MNRAS*, 402, 2049
 —. 2011a, *MNRAS*, 414, 2594
 —. 2011b, *A&A*, 525, A131
 —. 2012, *A&A*, 544, A90
 Howell, S. B., et al. 2014, *PASP*, 126, 398
 Huber, D., Stello, D., Bedding, T. R., Chaplin, W. J., Arentoft, T., Quirion, P., & Kjeldsen, H. 2009, *Communications in Asteroseismology*, 160, 74
 Huber, D., et al. 2010, *ApJ*, 723, 1607
 —. 2011, *ApJ*, 743, 143

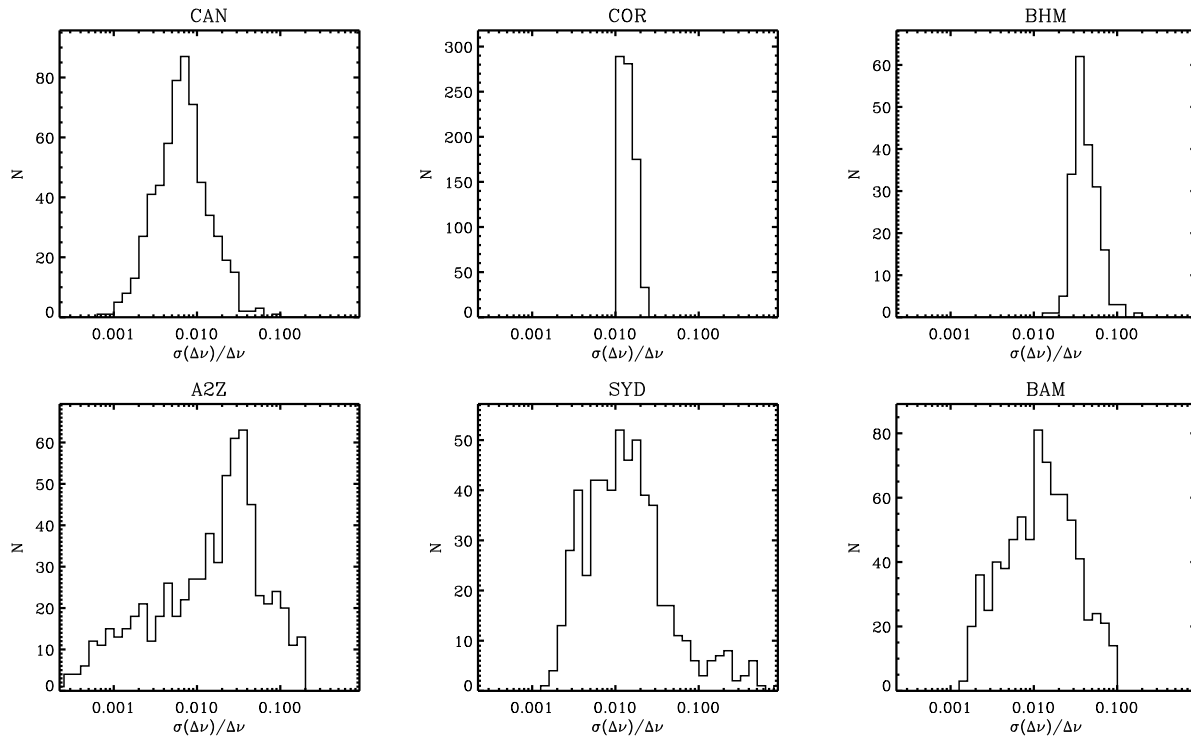


FIG. 9.— Relative uncertainty in $\Delta\nu$ reported by each pipeline. The scale on the abscissa is the same for all panels.

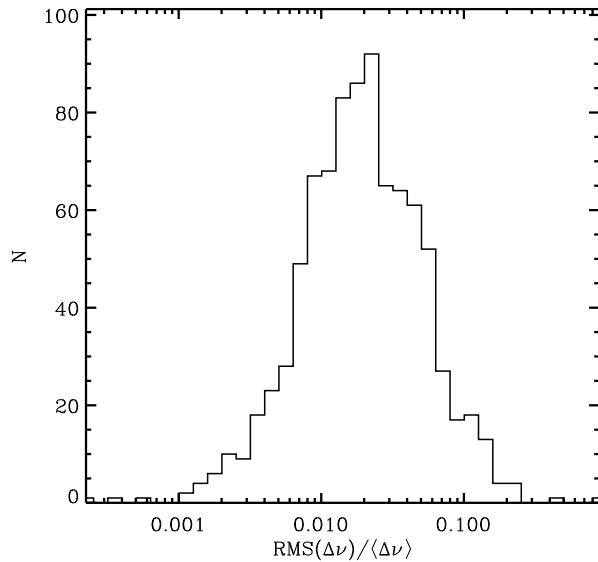


FIG. 10.— Relative RMS scatter of $\Delta\nu$ between all pipelines. Only stars for which at least two pipelines provided results are shown.

— 2014, *ApJS*, 211, 2

— 2016, *ApJS*, 224, 2

Jenkins, J. M., et al. 2010, *ApJ*, 713, L87

Kallinger, T., Hekker, S., Garcia, R. A., Huber, D., & Matthews, J. M. 2016, *Science Advances*, 2, 1500654

Kallinger, T., et al. 2010, *A&A*, 522, 1

— 2014, *A&A*, 570, 41

Kjeldsen, H., & Bedding, T. R. 1995, *A&A*, 293, 87

Majewski, S. R., Wilson, J. C., Hearty, F., Schiavon, R. R., & Skrutskie, M. F. 2010, in *IAU Symposium*, Vol. 265, *IAU Symposium*, ed. K. Cunha, M. Spite, & B. Barbuy, 480–481

Mathur, S., Garcia, R. A., Huber, D., Regulo, C., Stello, D., Beck, P. G., Houmani, K., & Salabert, D. 2016, *ArXiv e-prints*

Mathur, S., et al. 2010, *A&A*, 511, A46

— 2011, *ApJ*, 741, 119

Miglio, A., et al. 2012, *MNRAS*, 419, 2077

Mosser, B., & Appourchaux, T. 2009, *A&A*, 508, 877

Mosser, B., et al. 2010, *A&A*, 517, 22

— 2012, *A&A*, 537, A30

Pinsonneault, M. H., et al. 2014, *ApJS*, 215, 19

Sharma, S., Bland-Hawthorn, J., Johnston, K. V., & Binney, J. 2011, *ApJ*, 730, 3

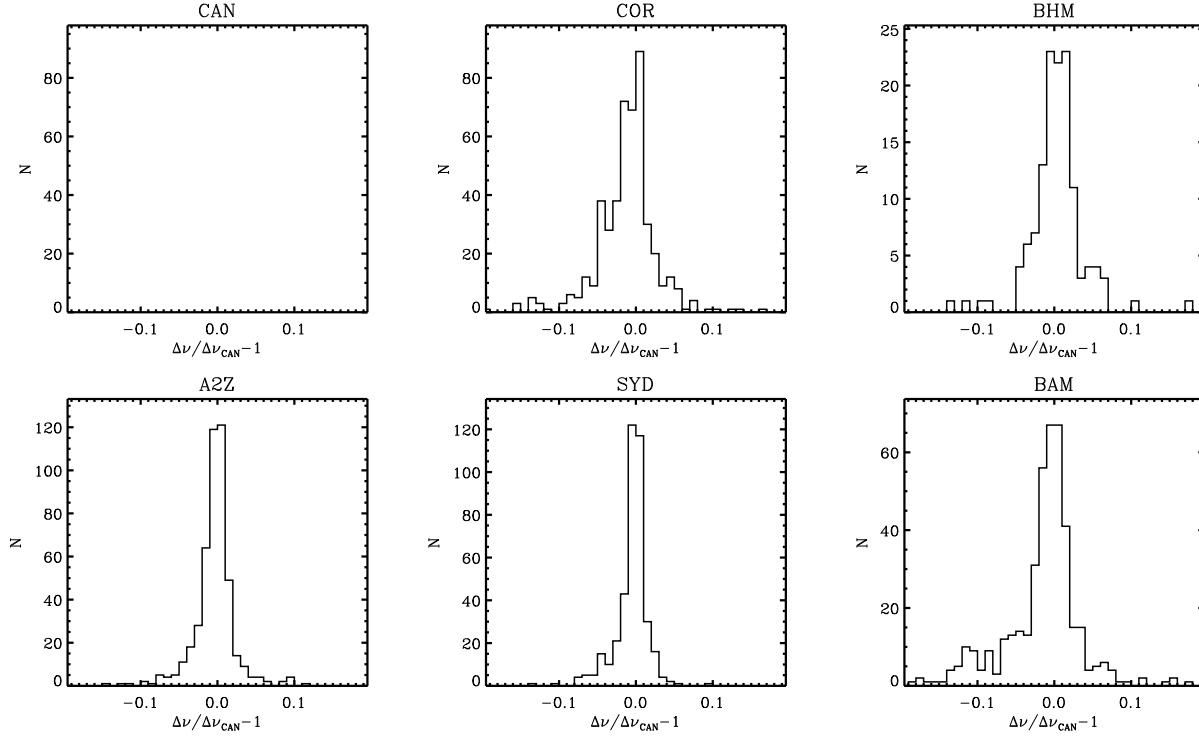


FIG. 11.— $\Delta\nu$ relative to the CAN pipeline result. Only stars in common with the CAN list are shown.

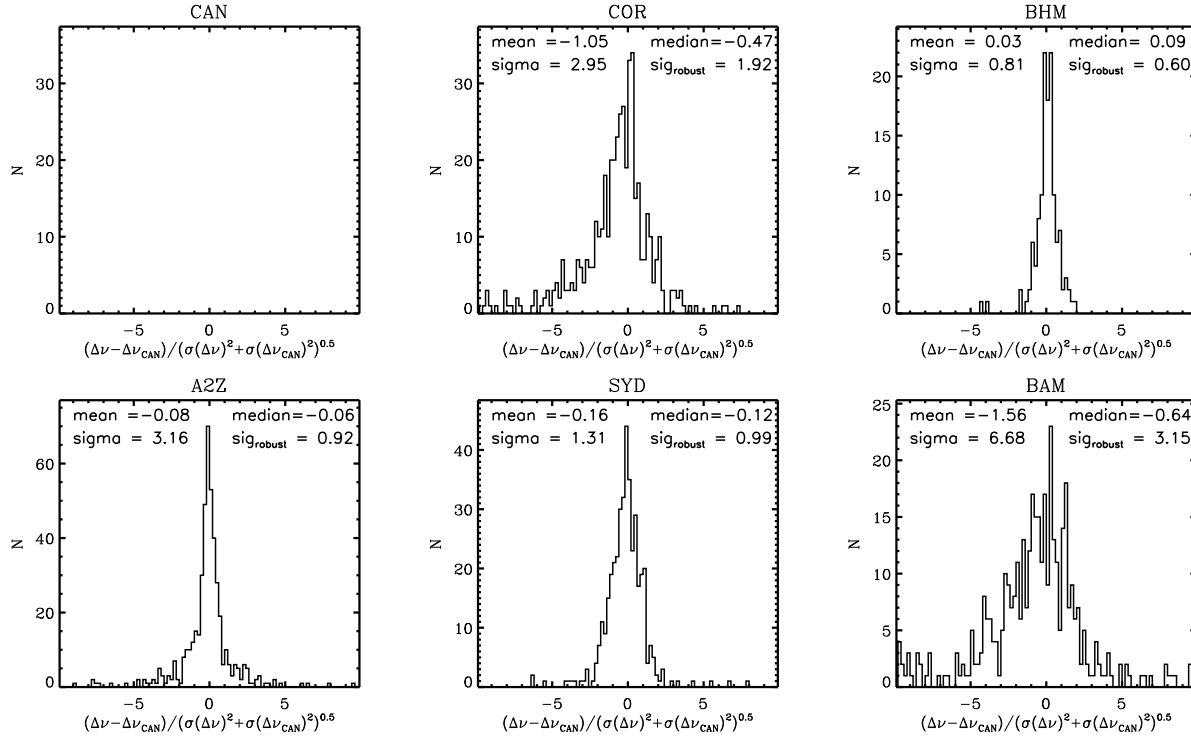


FIG. 12.— $\Delta\nu$ deviation from CAN pipeline result relative to quadrature uncertainty between the two pipelines. Only stars in common with the CAN list are shown. Straight mean and standard deviation is shown in addition to the median and robust standard deviation of the distributions.

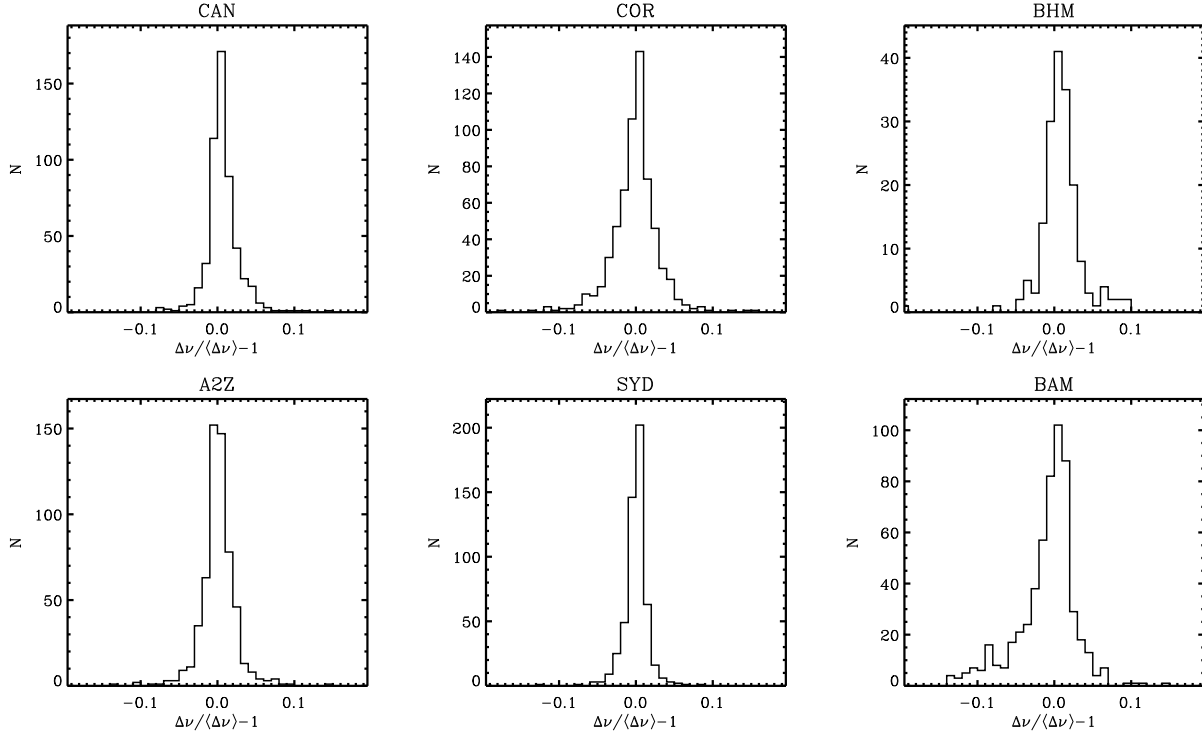


FIG. 13.— $\Delta\nu$ relative to the mean across all pipelines. Only stars for which at least two other pipelines provided results are shown.

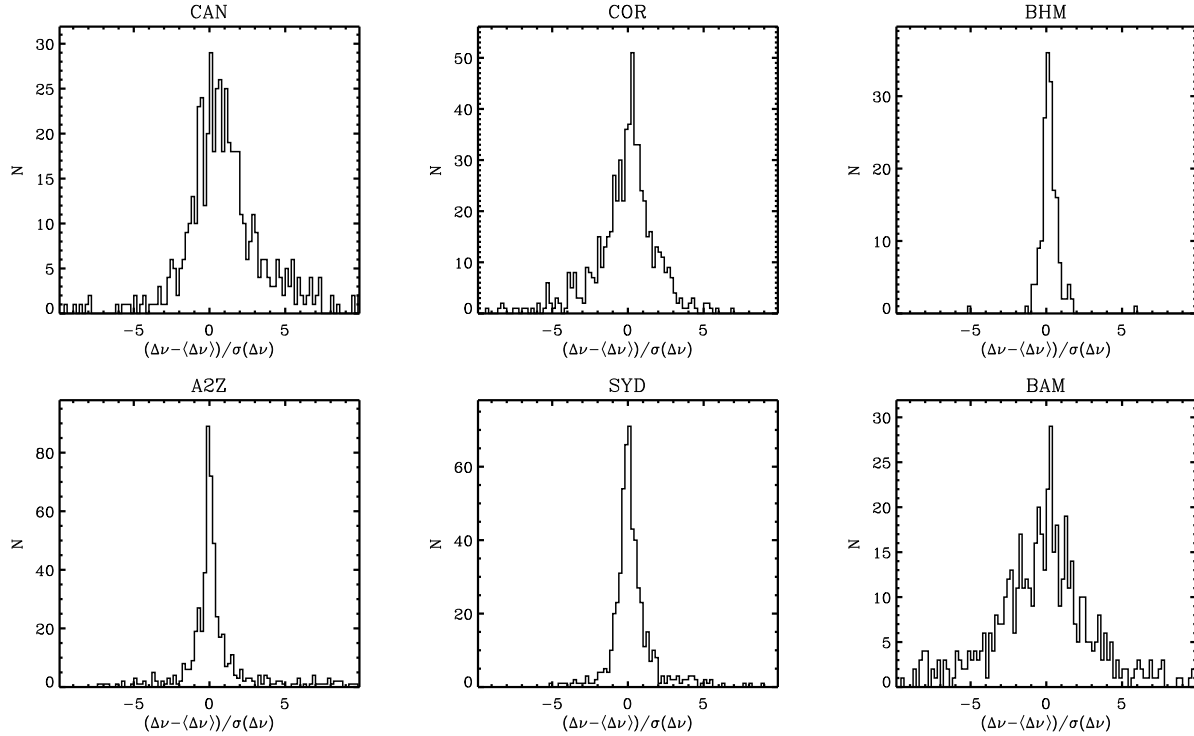
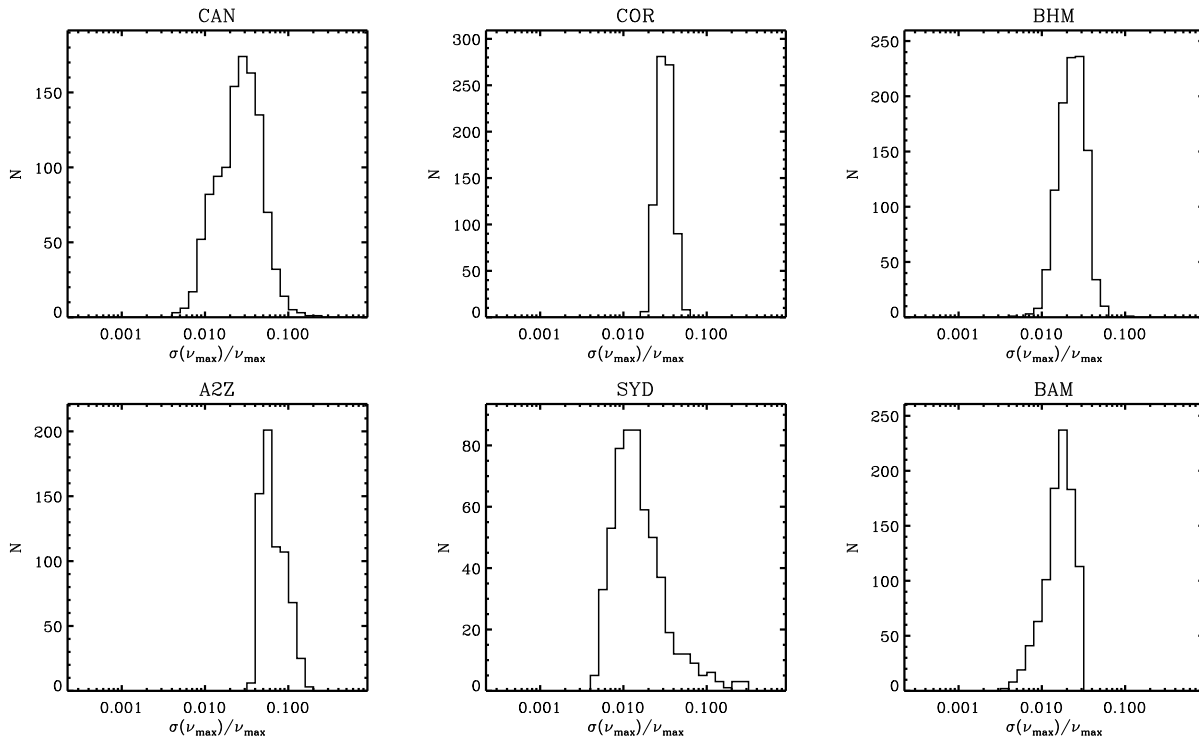
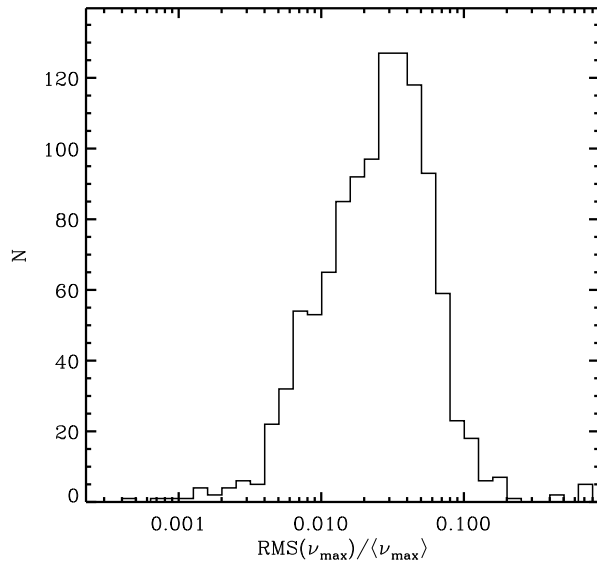


FIG. 14.— $\Delta\nu$ deviation from mean across all pipelines relative to the uncertainty from the individual pipeline. Only stars for which at least two other pipelines provided results are shown.

FIG. 15.— Relative uncertainty in ν_{\max} .FIG. 16.— Relative RMS scatter of ν_{\max} between all pipelines. Only stars for which at least two pipelines provided results are shown.

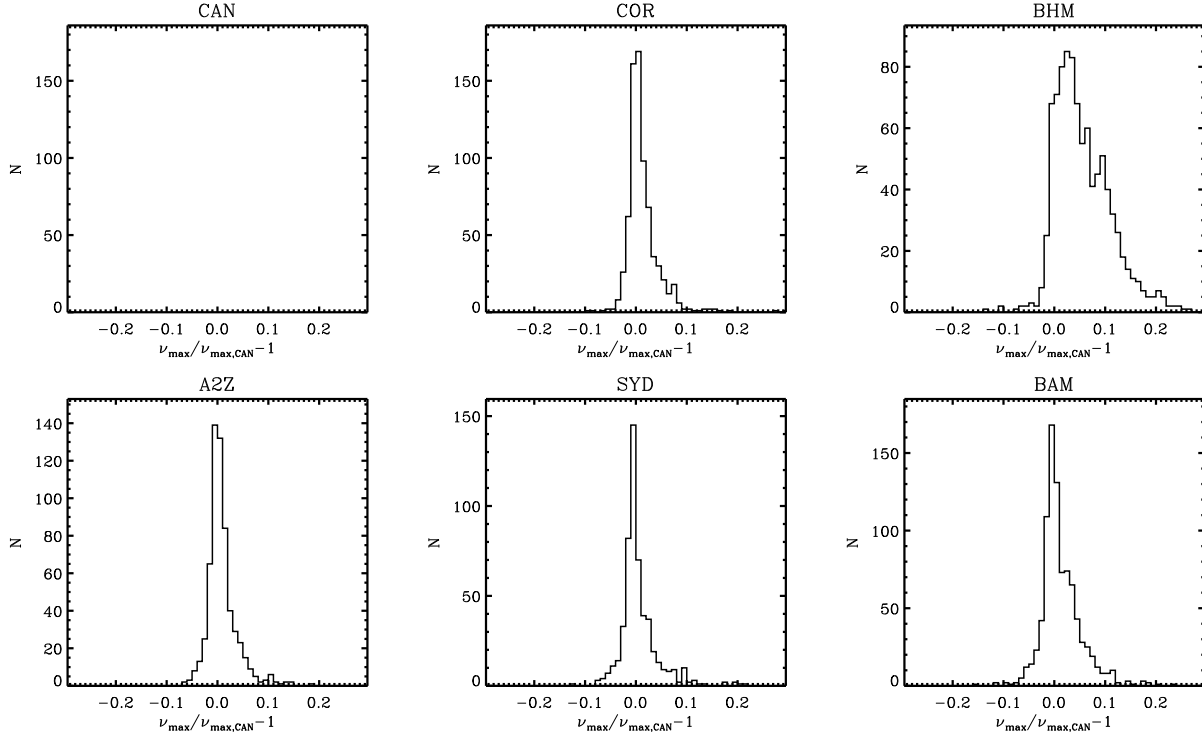


FIG. 17.— ν_{\max} relative to the CAN pipeline result. Only stars in common with the CAN list are shown.

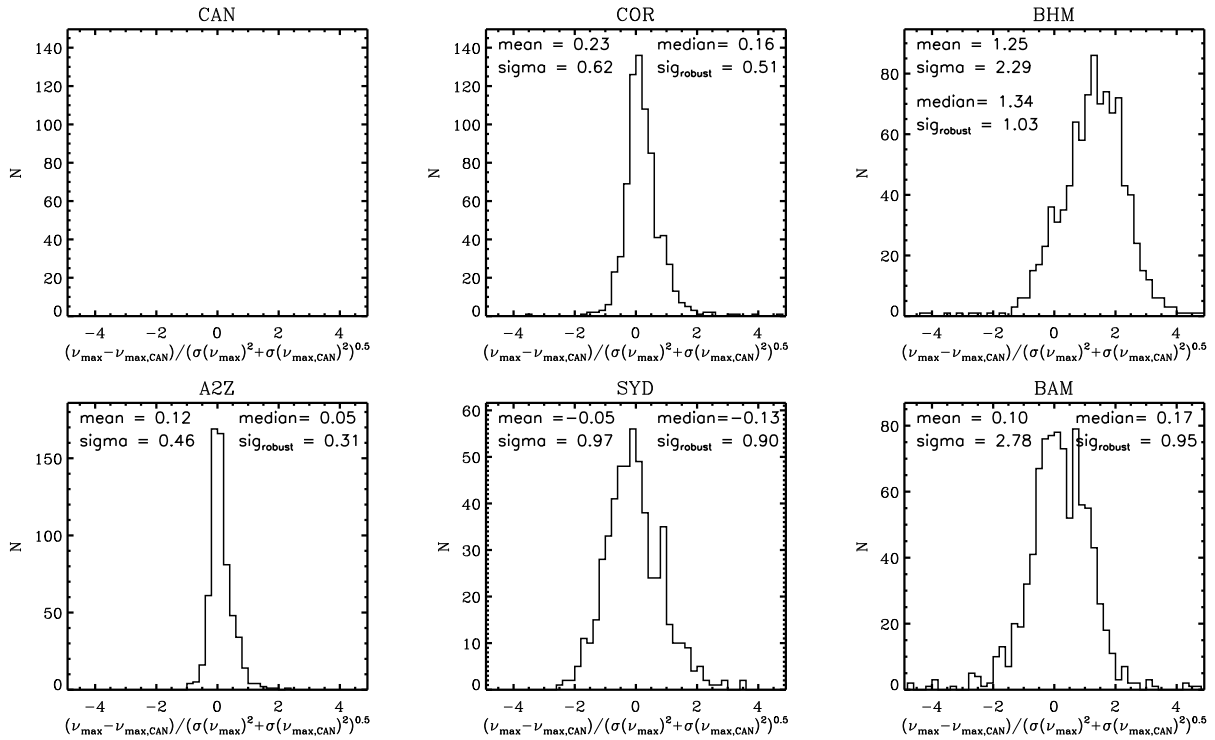


FIG. 18.— ν_{\max} deviation from CAN pipeline result relative to quadrature uncertainty between the two pipelines. Only stars in common with the CAN list are shown. Straight mean and standard deviation is shown in addition to the median and robust standard deviation of the distributions.

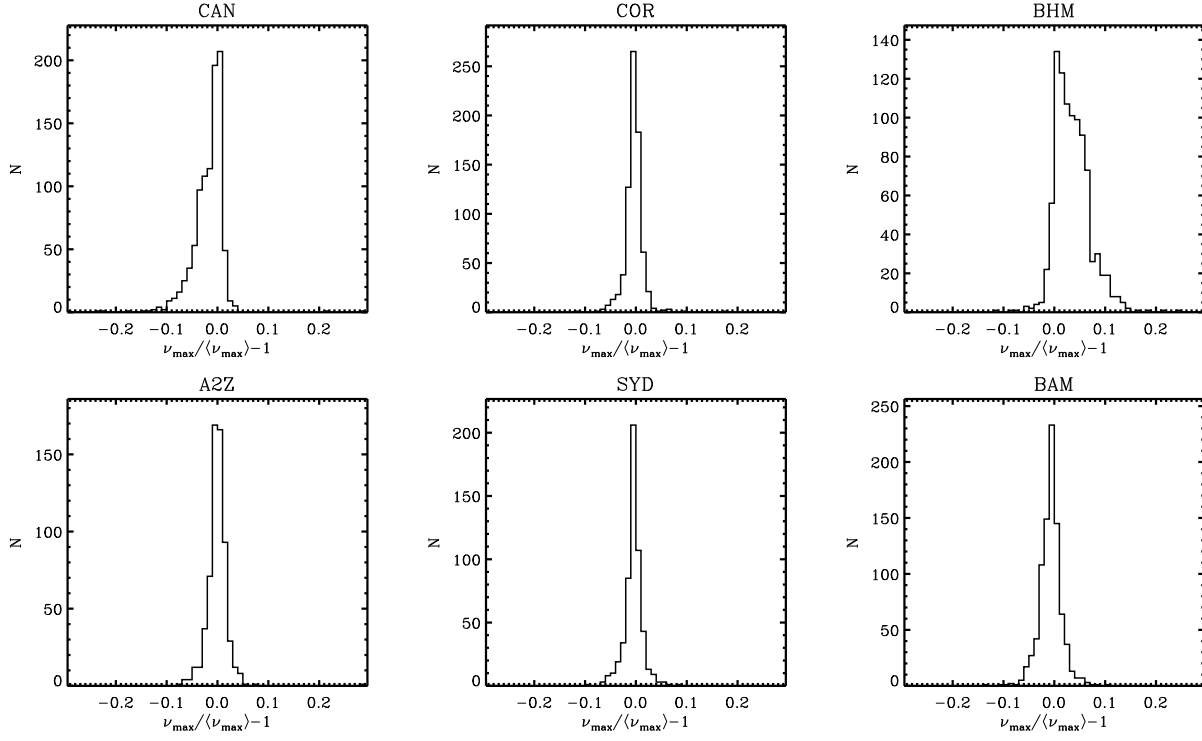


FIG. 19.— ν_{\max} relative to mean across all pipelines. Only stars for which at least two other pipelines provided results are shown.

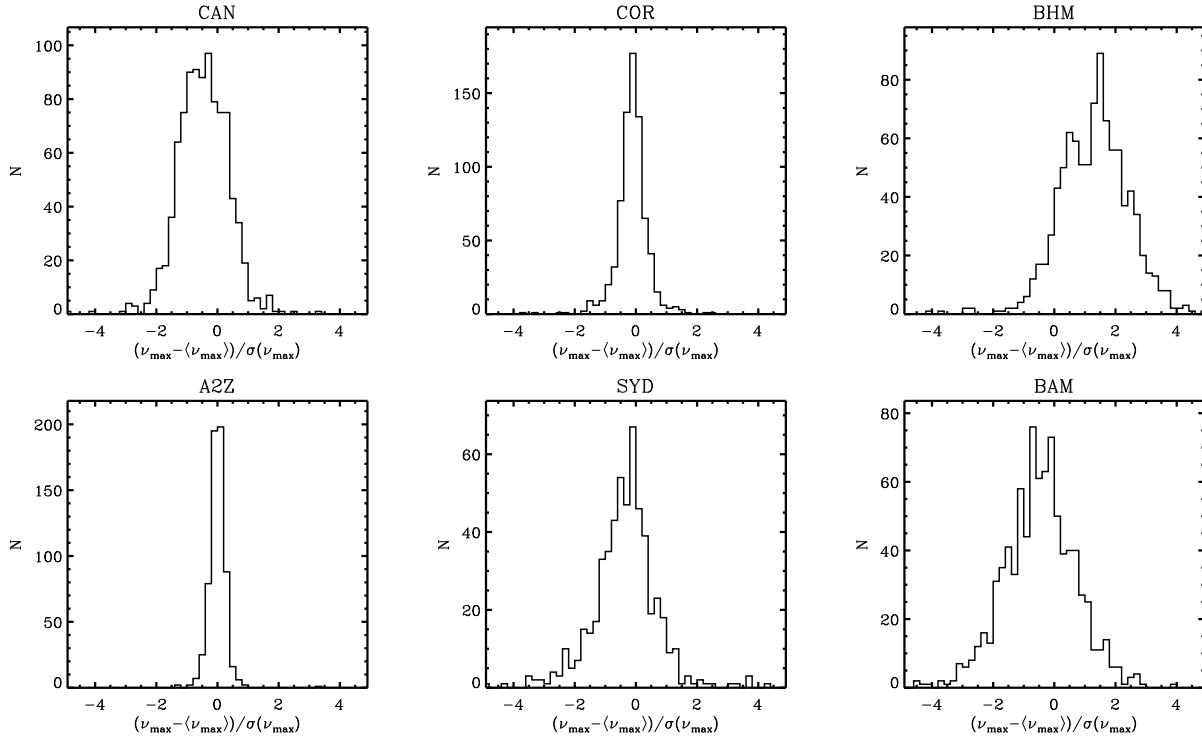


FIG. 20.— ν_{\max} deviation from mean across all pipelines relative to the uncertainty from the individual pipeline. Only stars for which at least two other pipelines provided results are shown.